TÜBİTAK

Turkish Journal of Earth Sciences

http://journals.tubitak.gov.tr/earth/

Research Article

Turkish J Earth Sci
(2021) 30: 279-312

doi:10.3906/yer-2005-6

Peritectic assemblage entrainment and mafic–felsic magma interaction in the Late Oligocene–Early Miocene Karadağ Pluton in the Biga Peninsula, northwest Turkey: petrogenesis and geodynamic implications

Namık AYSAL[1,*], Abdullah Sinan ÖNGEN[1], Sabah YILMAZ ŞAHİN[1], Cem KASAPÇI[1], Nurullah HANİLÇİ[1], Irena PEYTCHEVA[2]

[1]Department of Geological Engineering, İstanbul University-Cerrahpaşa, İstanbul, Turkey
[2]Geological Institute, Bulgarian Academy of Sciences, Sofia, Bulgaria

Received: 04.05.2020 • **Accepted/Published Online:** 04.11.2020 • **Final Version:** 22.03.2021

Abstract: The Hellenic subduction system governs the entire Aegean region through the creation of a migrating magmatic arc that has existed since the beginning of the Early Cenozoic. The Karadağ Pluton is situated in the NW part of Turkey and represents one of the distinct snapshots of this subduction system during the Late Oligocene-Early Miocene Period.iod. It consists of 2 major lithological units, based on their petrographic and geochemical features, comprising: 1) main plutonic facies (SiO_2 < 70 wt.%) that are dominated by hornblende- and biotite-bearing monzogranite, quartz monzonite, and granodiorite, and 2) late-stage more felsic facies (SiO_2 > 70 wt.%) that are represented by cordierite-free and cordierite-bearing leucogranites. Zircon U-Pb laser ablation inductively-coupled plasma mass spectrometry and K-Ar dating revealed crystallization and cooling ages of 23.9 ± 0.5 Ma and 20.2 ± 0.9 Ma for the main plutonic bodies, and 22.0 ± 1.1 Ma for the leucogranite facies, respectively. The pluton had a high-K calc-alkaline affinity and exhibited a metaluminous to peraluminous (aluminum saturation index of <1.1), and displayed an I-type character. It was enriched with large ion lithophile elements and light rare earth elements, and it was depleted of high field strength elements with negative Eu anomalies. In the tectonic setting discrimination diagrams, all of the granite samples fell into the volcanic arc granite and syn-collisional granite fields. The initial Sr-Nd isotope data of the pluton were compatible with an enriched mantle source. Petrographic and geochemical features indicated that it has been affected by multiple magma evolution processes, such as fractional crystallization, magma mixing, and assimilation. Moreover, the pluton displayed source heterogeneities and peritectic mineral entrainment, such as the coexistence of K-feldspar and cordierite, which could be interpreted as incongruent melting of the crust in the fluid-present system. The petrological and geochemical data suggested that the Karadağ Pluton formed by the mixing of mantle-derived mafic and crustal-derived felsic magmas at shallow crustal levels, mainly derived by the partial melting events related to the northward subduction of the Hellenic slab beneath the Sakarya Zone.

Key words: Peritectic entrainment assemblage, magma mixing, U/Pb and K-Ar dating, mantle-crust interaction, Biga Peninsula, Sakarya Zone

1. Introduction

The mineralogical composition, textural, and geochemical features of granitic rocks play an important role in understanding the petrological evolution of the continental crust and source characteristics of the generated magma. Granitic magmas can be derived from partial melting of different types of protoliths or result as the end-products of differentiation of mafic magmas (Clemens and Stevens, 2012). Granitic intrusions and their volcanic equivalents constitute the main bulk of the continental crust in many places around the world. Magma generation in the continental crust may develop due to thickening of the crust in collision zones, hybridization between crustal- and mantle-derived magmas in the continental arc margin, and/or anatexis of crustal protoliths (Bartoli et al., 2016 and references therein). Field geology, petrography, whole-rock geochemistry, isotope ratio, and mineral chemistry data aid in understanding the generation of granitic magma, their physicochemical conditions, tectonic settings, and source protolith. However, there are still contradictory views about the melting processes at the source and the magma evolution processes (i.e. fractional crystallization (FC), mixing-mingling, assimilation combined FC (AFC)) that affect the chemistry of granitic rocks during the ascent or emplacement of magma (Bartoli et al., 2016 and references therein). Parental magma can be contaminated by assimilation of country-rock and/or different magma mixing-mingling processes in open magmatic systems. Ac-

* Correspondence: aysal@istanbul.edu.tr

cording to some studies, crystals and melts may separate from the parental magma by the separation of entrained restite, gravitational crystal settling, or wall-rock accumulation in a closed system, or by mechanisms, such as filter-pressing processes or in situ crystallization, in intermediate and felsic magmas (Tindle and Pearce, 1981; Walker and Carr, 1986; Blevin and Chappell, 1992; Dias and Leterrier, 1994; Claeson and Meurer, 2004; Rezaei-Kahkhaei et al., 2011). The presence of peritectic mineral assemblages, such as cordierite, garnet, and orthopyroxene, may explain fluid-present or fluid-absent melting conditions, wall-rock assimilation, and source rock composition (Clarke, 1995). The volcano-plutonic belt of NW Anatolia consists of Early Eocene to Late Miocene volcano-sedimentary sequences and their coevally developed plutons, which display typical high-K calc-alkaline and I-type geochemical characters, and gradually young southward along the Aegean region (Pe-Piper and Piper, 1989; Aysal, 2015; Ersoy et al., 2017 and references therein). The closure of the Neo-Tethyan Ocean and subsequent arc-continent collision caused the development of syn to postcollisional magmatic belts during the Middle Eocene (Harris et al., 1994; Delaloye and Bingöl 2000; Köprübaşı and Aldanmaz, 2004; Altunkaynak et al., 2012; Ersoy and Palmer, 2013; Aysal, 2015 and references therein). Magmatic activity during the Late Oligocene and Early Miocene is represented by the widespread intermediate to felsic plutonic rocks and its volcanic equivalents in NW Turkey, particularly in the Biga Peninsula. The Upper Miocene-Pliocene magmatic activity consists of alkaline-basic volcanics (Aysal, 2015 and references therein). Aysal (2015) suggested that the Oligo-Miocene plutonism in the Biga Peninsula may be related to crustal thinning after the retreat and roll-back of the Hellenic Slab.

In this paper, new zircon U/Pb and whole-rock/mineral K-Ar ages, whole-rock -geochemistry, mineral chemistry, and Sr-Nd isotope data from the Karadağ Pluton, located in the Sakarya Zone (Figure 1), were presented in order to better understand its unusual mineral assemblage, which comprises major granitic and peritectic/metamorphic minerals, and magma evolution processes, such as FC, magma mixing-mingling and AFC during magma ascent and emplacement. Herein, also discussed were the crystallization conditions, such as the emplacement depth,

Figure 1. Major crustal fragments and Tethyan suture belts of Turkey (Okay and Tüysüz, 1999), and location of the study area. IPS: Intra-Pontide Suture, IAES: İzmir-Ankara-Erzincan Suture, ITS: Inner-Tauride Suture.

temperature, oxygen fugacity ($\log fO_2$), and water content (H_2O_{melt}) of the parental magma of the Karadağ Pluton within the related tectonic settings.

2. Geology and petrography

2.1. Geological setting and field observations

The Karadağ Pluton has intruded into the basement rocks of the Sakarya Zone and its cover units (Figure 1). The basement rocks of the Sakarya Zone in the study area comprise pre-Jurassic metamorphics (the Karakaya Complex represented by the Orhanlar Greywacke) and Jurassic-Cretaceous cover units (i.e. the Bayırköy Formation and the Bilecik Limestone; Figure 2). The Orhanlar Greywacke consists of greywacke, sandstone, conglomerate, limestone, and black radiolarian ribbon chert (Okay et al., 2011).

The Orhanlar Greywacke is unconformably overlain by the Bayırköy Formation and Bilecik Limestone (Altınlı, 1973). The Liassic Bayırköy Formation is composed of quartzofeldspathic conglomerate, sandstone, siltstone, and claystone. The late Jurassic–late Cretaceous Bilecik Limestones (Altınlı, 1973) are composed of neritic and pelagic carbonates. The Bilecik Limestone is unconformably overlain by the Upper Oligocene-Miocene volcanic and volcaniclastic rocks. This volcanic succession, which comprises mainly andesitic lava flows, agglomerate, and tuff, is unconformably overlain by Cenozoic coal bearing continental clastics and Quaternary alluvium deposits.

The main body of the Karadağ Pluton comprises granodiorite, quartz-monzonite, and monzogranite lithologies (Figure 3). In general, the majority of these lithologies are medium- to coarse-grained and have porphyritic, equigranular, and hypidiomorphic textures (Figures 3a–3c), and only rarely display foliation at the pluton margins. The porphyritic texture is defined by randomly oriented euhedral to subhedral large plagioclase and orthoclase megacrysts in a matrix composed of fine-grained quartz, K-feldspar, plagioclase, hornblende, and biotite (Figure 3c). These different lithologies contain mafic microgranular (magmatic) enclaves (MMEs) of hypabyssal rocks (Figures 3a and 3c). Some of the K-feldspar and plagioclase megacrystals are euhedral and subhedral prismatic in shape, and their grain sizes reach up to 3–6 cm in length (Figures 3d, 3e, 3g, and 3h). They contained plagioclase, biotite, hornblende, and opaque mineral inclusions. Minerals such as zircon, apatite, titanite, and magnetite are found as accessory phases. Leucocratic facies of the pluton include nodular tourmaline minerals in some places. This facies crosscuts the pluton and has sharp contacts with the main plutonic body (Figures 3f and 3i).

The Karadağ Pluton created a contact metamorphic aureole around the sedimentary rocks of Orhanlar Greywacke and Bayırköy Formation, which were then turned into hornfels. The main mineral composition of the hornfels is quartz, K-feldspar, plagioclase, muscovite, biotite, actinolite, epidote, and chlorite.

2.2. Petrographical features

The main mineralogical assemblage of the pluton comprised quartz (15%–40%), plagioclase (25%–45%), K-feldspar (15%–30%), hornblende (5%–15%), and biotite (5%–10%) (Figures 4a–4c). The secondary mineral phases comprised chlorite, epidote, calcite, and clay. The MMEs had a quartz-microdioritic or microdioritic composition, and were separated from the host rocks by more mafic mineral contents and microgranular textures (Figures 4d and 4e). Some magma mixing textures were determined under the microscope, such as rapakivi, antirapakivi, boxy and spongy-cellular plagioclase, poikilitic K-feldspar, blade-shaped biotite, acicular apatite, feldspar-biotite ocellar, appinitic, titanite-centered, and biotite destabilization, in both the MMEs and their host rocks (Figures 4d and 4e). There were also mixing-related textures, which will be explained in the petrogenesis section. The leucocratic facies and aplitic-pegmatitic vein rocks were pinkish grey to white and display fine- to medium-grained equigranular and granophyric textures (Figure 4f). These rocks consisted of quartz, K-feldspar, plagioclase, rare biotite, and cordierite, and they randomly contained large tourmaline crystals that had developed in late-stage miarolitic cavities (Aysal et al., 2020). The cordierites mainly displayed subhedral to anhedral shapes. They showed weak cleavage and large subconchoidal fractures. Some of the cordierites contained mineral inclusions such as quartz, opaque minerals, and were rarely affected by pinitic alteration along the crystal margins and fractures.

3. Materials and methods

3.1. Geochronology

A granite sample from the main body of the Karadağ Pluton was selected for zircon U-Pb geochronology, and 4 samples were selected from the main plutonic body and leucogranitic facies for K-Ar geochronology. Separated zircon grains in the range of 63 to 125 μm from each sample were mounted in epoxy resin and imaged by cathodoluminescence (CL) at the scanning electron microscopy laboratory of Belgrade University (Serbia), using a JEOL JSM-6610LV scanning electron microscope (Akishima, Tokyo, Japan). The selected zircon grains were dated using U-Th-Pb laser ablation-ICP-MS (LA-ICP-MS) at the Geological Institute of the Bulgarian Academy of Science in Sofia, Bulgaria, following the method of U-Pb dating outlined by Aysal et al. (2018). The K-Ar ages were determined at the Institute of Geological Sciences of the Polish Academy of Sciences in Krakow, Poland, following the method of Yılmaz Şahin et al. (2012).

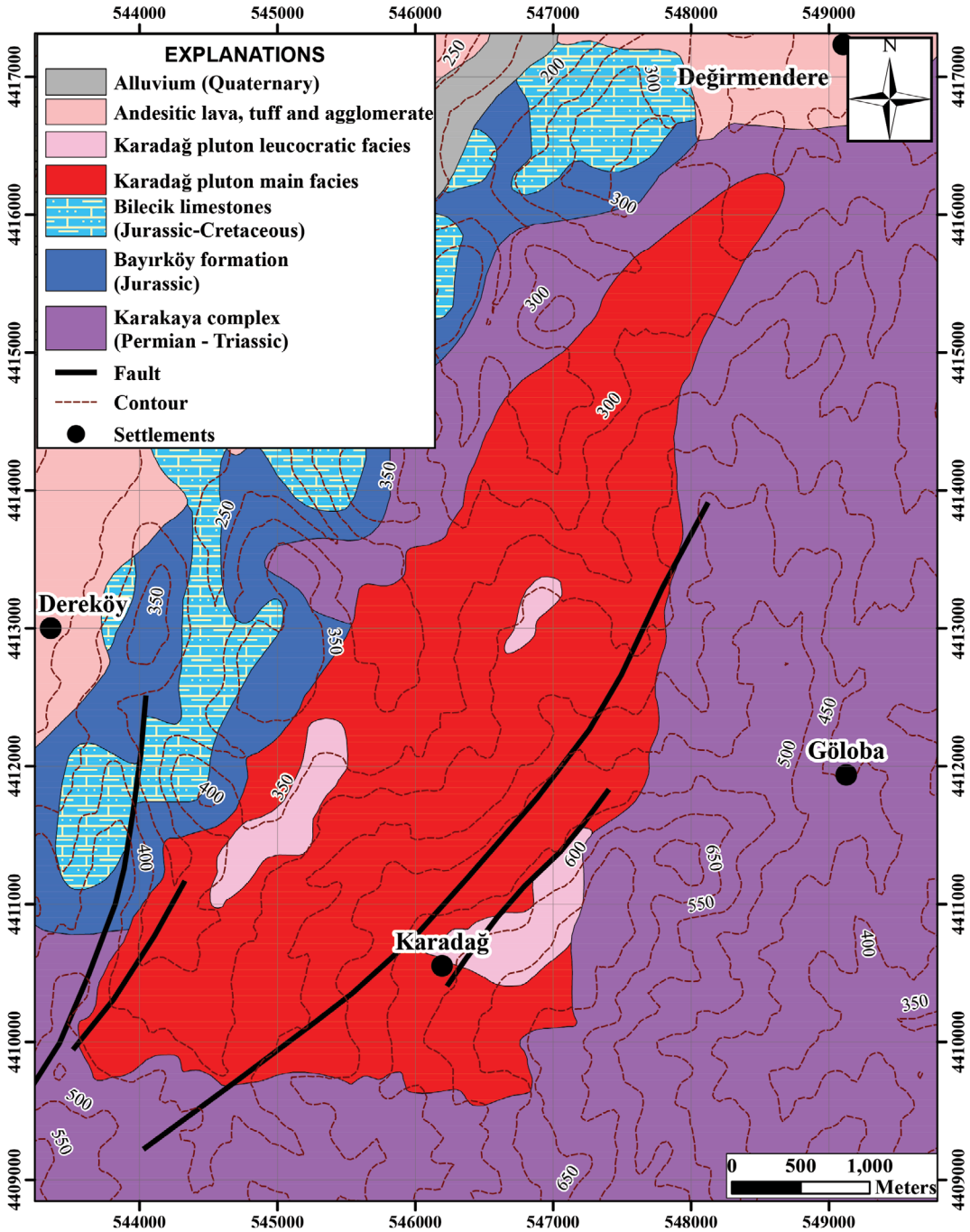

Figure 2. Geological map of the Karadağ Pluton and surrounding areas (coordinate system: WGS1984_UTM_Zone 35N).

3.2. Whole-rock geochemistry

A total 18 rock samples were selected from the Karadağ Pluton (9 samples from the main plutonic body, and 9 samples from the leucogranite facies) for the whole-rock geochemical analyses. Selected samples were ground down to finer than 800 mesh, and the experimental analyses were conducted at Acme Analytical Laboratories Ltd., in Vancouver, Canada. The analyses were conducted using ICP-atomic emission spectrometry after $LiBO_2$ fusion for all of the major oxides. The analytical precision was ±

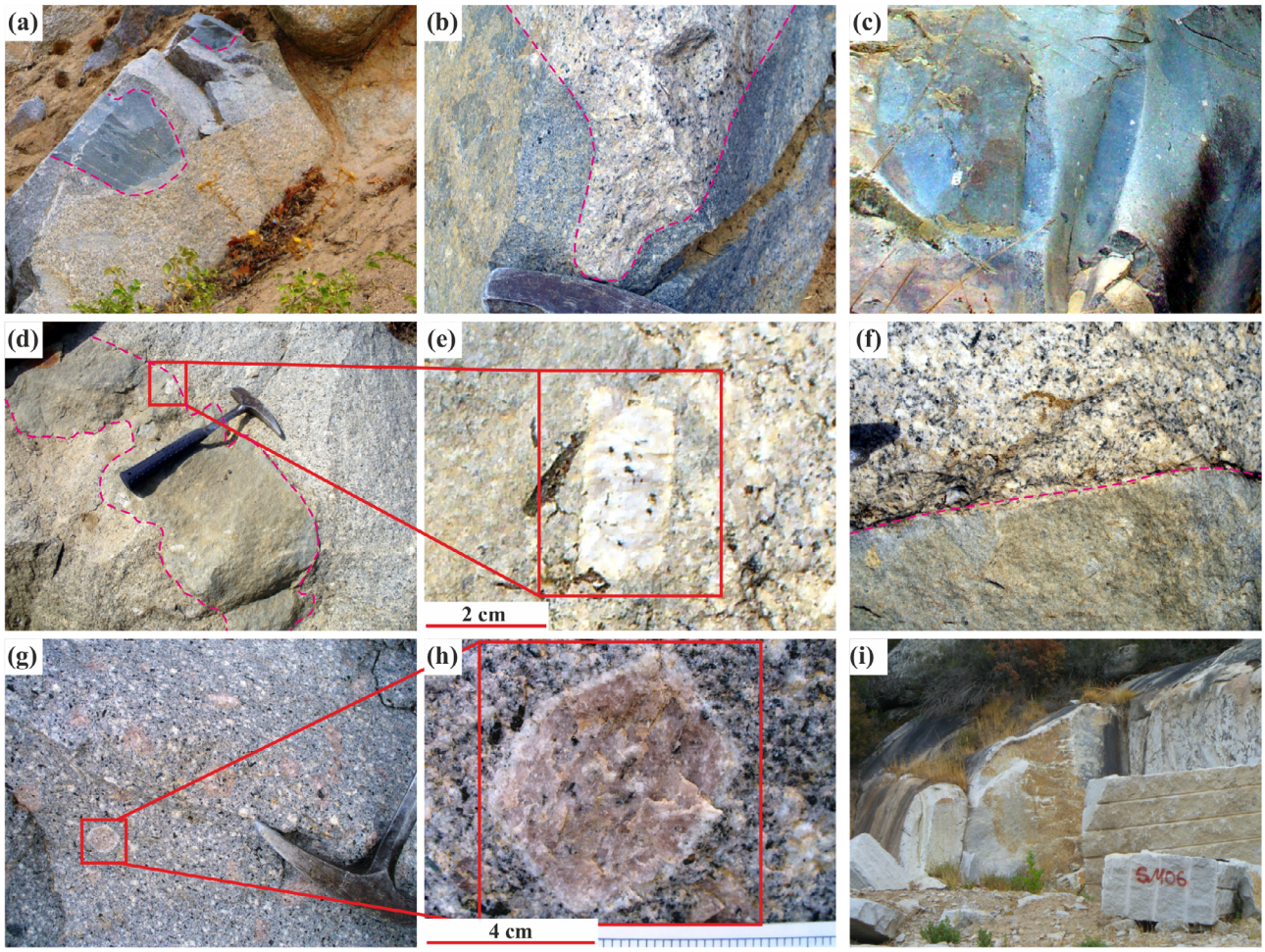

Figure 3. Representative field photographs of various rock-types from the Karadağ Pluton: a) MMEs, b) amalgamation of 2 compositionally and texturally different magmas, c) close-up view of a MME with large plagioclase megacrysts, d) boundary of microgranular and coarse-grained monzonitic magmas with large plagioclase megacrysts, e) close-up view of plagioclase megacryst, f) sharp contact between the microgranular and coarse grained magmas, g) monzogranite containing coarse K-feldspar xenocrysts with rapakivi texture, and h) close view of K-feldspar xenocryst with rapakivi texture, i) leucocratic facies of the Karadağ Pluton.

0.01% for the major oxides, except for Fe_2O_3, which was ± 0.04% (detection limits were 0.01%). Sample preparations for the trace elements, rare earth elements (REEs), and incompatible elements were performed using $LiBO_2$ fusion, while aqua-regia digestion was implemented for the precious and base metals. The prepared samples were analyzed using ICP-MS. The analytical precision values were better than 1% for the REEs (detection limits were 0.01–0.3 ppm) and better than 1% for all of the other trace elements (detection limits were 0.1–1 ppm). The loss-on-ignition (LOI) was given as the weight difference after ignition at 1050 °C. The total iron concentration was determined from the Fe_2O_3. All of the samples were analyzed using the STD-SO-17 international standard.

3.3. Sr-Nd isotopes

Two samples from the main plutonic body and 1 sample from leucogranite facies were selected from the Karadağ Pluton for the Sr-Nd isotope analyses. The Sr and Nd isotope analyses were performed at the Central Laboratory of the Middle East Technical University, in Ankara, Turkey, following the method of Aysal et al. (2012).

3.4. Mineral chemistry

Mineral chemistry analyses were performed using a CAMECA SX-100 (including 4 wavelength-dispersive detectors and 1 energy-dispersive detector) electron microprobe (Gennevilliers, France). The electron probe micro analyses (EPMA) were performed at the Prof. Adnan Tekin Materials Science and Production Technologies Applied Re-

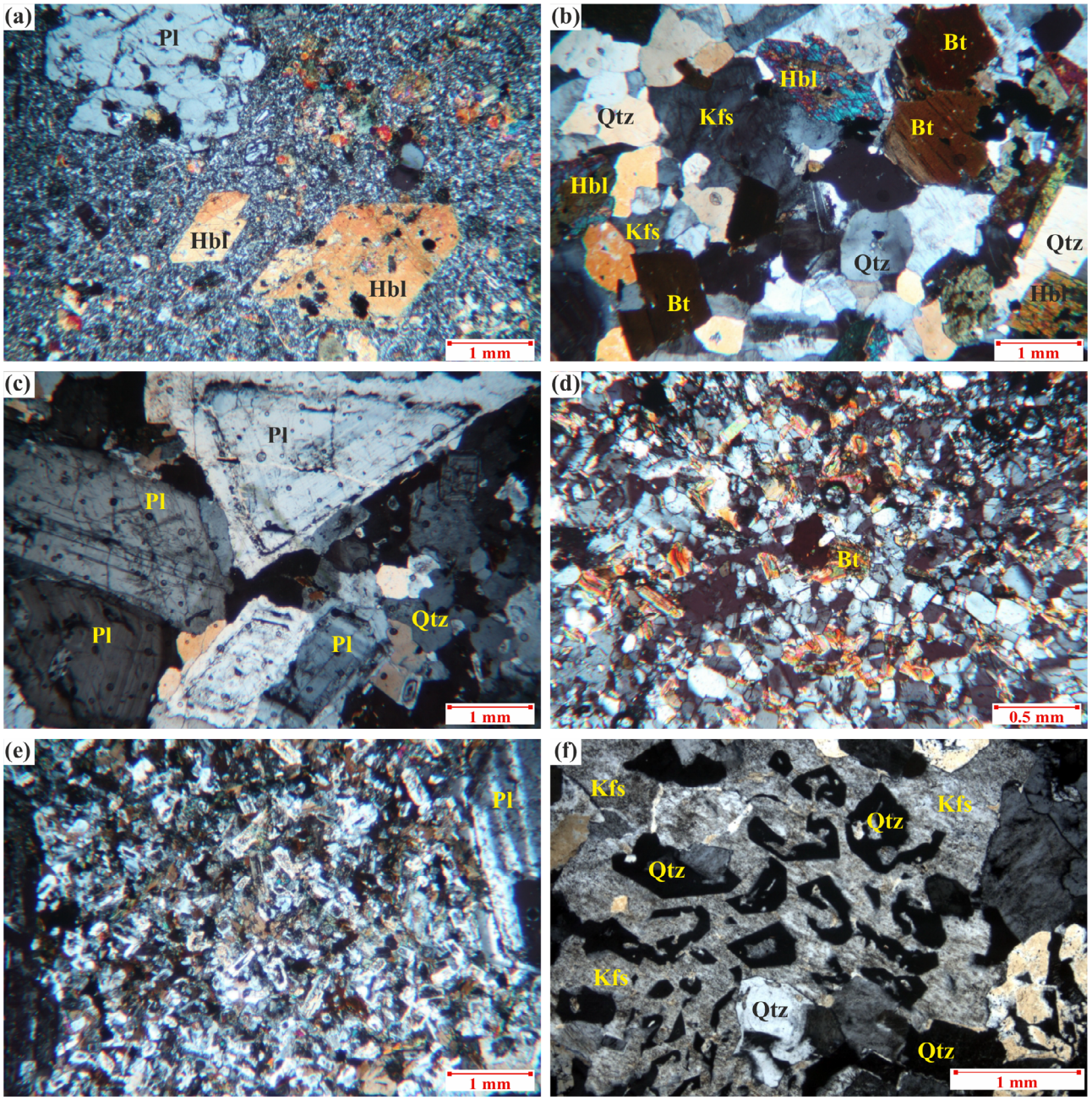

Figure 4. Representative thin-section photographs of various rock-types from the Karadağ Pluton: a) porphyritic texture at the pluton margin, b) granular and c) hypidiomorphic texture of the monzonite, d) biotite-rich and hornblende-biotite bearing, e) fine-grained MMEs, and f) granophyric leucogranite, quartz crystal inclusions in K-feldspar. Hbl: hornblende; Pl: plagioclase; Kfs: K-feldspar; Bt: biotite; Qtz: quartz.

search Center of İstanbul Technical University, in İstanbul, Turkey. The analyses were performed using an accelerating voltage of 15 kV, beam current of 20 nA, counting interval of 13 s, and beam size of 3 μm. The precision of the method was < 0.5% for all of the measured concentrations.

4. Results

4.1. U-Pb zircon crystallization and K-Ar cooling ages

The zircon grains from the Karadağ Pluton samples were primarily colorless or pale brown, transparent, and occurred as euhedral prismatic crystals (50–150 μm). The CL

images demonstrated a clear magmatic oscillatory zoning pattern for all of the zircons (Figure 5), with visible inherited cores in some grains. Th/U ratios of the zircons varied between 0.35 and 0.87 (average 0.60), which was consistent with a magmatic origin. The analyses of the zircons from the main plutonic body (sample DG-5) yielded $^{206}Pb/^{238}U$ ages of 22.60 ± 1.03 Ma to 27.05 ± 0.77 Ma (Table 1), a concordia age of 23.63 ± 0.17 Ma, and weighted average of 23.90 ± 0.42 Ma. The K-Ar analyses on the separated hornblende, biotite, and whole-rock samples from the Karadağ Pluton yielded cooling ages that ranged from 20.2 ± 0.9 to 23.9 ± 0.5 Ma, respectively (Table 2).

4.2. Major and trace elements

Major and trace element data of the representative samples from the Karadağ Pluton are presented in Table 3. Normative compositions of the pluton were plotted on a Q'-ANOR diagram for classifying the samples (Streckeisen and Le Maitre, 1979). In that diagram, samples from the Karadağ Pluton were classified as granodiorite, monzogranite, syenogranite, and quartzmonzonite (Figure 6a). The SiO_2 contents of the samples displayed a wide range between 60.95 to 77.75 wt.%. In the diagrams, intermediate (SiO_2 < 70 wt.%, red square) and leucogranite (SiO_2 > 70 wt.%, blue circle) facies were plotted by 2 different symbols. Note that there was a prominent gap between 60.95 and 67.09 wt.% SiO_2, separating the granodiorite and monzogranites. Almost all of the samples fell into the high-K calc-alkaline field in the K_2O vs. SiO_2 classification diagram (Figure 6b) of Peccerillo and Taylor (1976). The Karadağ Pluton samples had a slightly metaluminous to peraluminous character, with aluminum saturation index (ASI) (the molecular ratio Al / (Ca – 1.67P + Na + K)) values of 0.79–1.08 (ASI < 1.1), which fell within the field of I-type granites (Maniar and Piccoli, 1989; Figure 6c). Samples of the Karadağ Pluton were classified as metaluminous, low to felsic peraluminous fields in the B (Fe+Mg+Ti) vs. A (Al – (K+Na+2Ca) classification diagram (Figure 6d) of Debon and Le Fort (1983) (modified by Villaseca et al., 1998). These samples showed contrasting differentiation trends between mesocratic to leucocratic fields, as displayed by

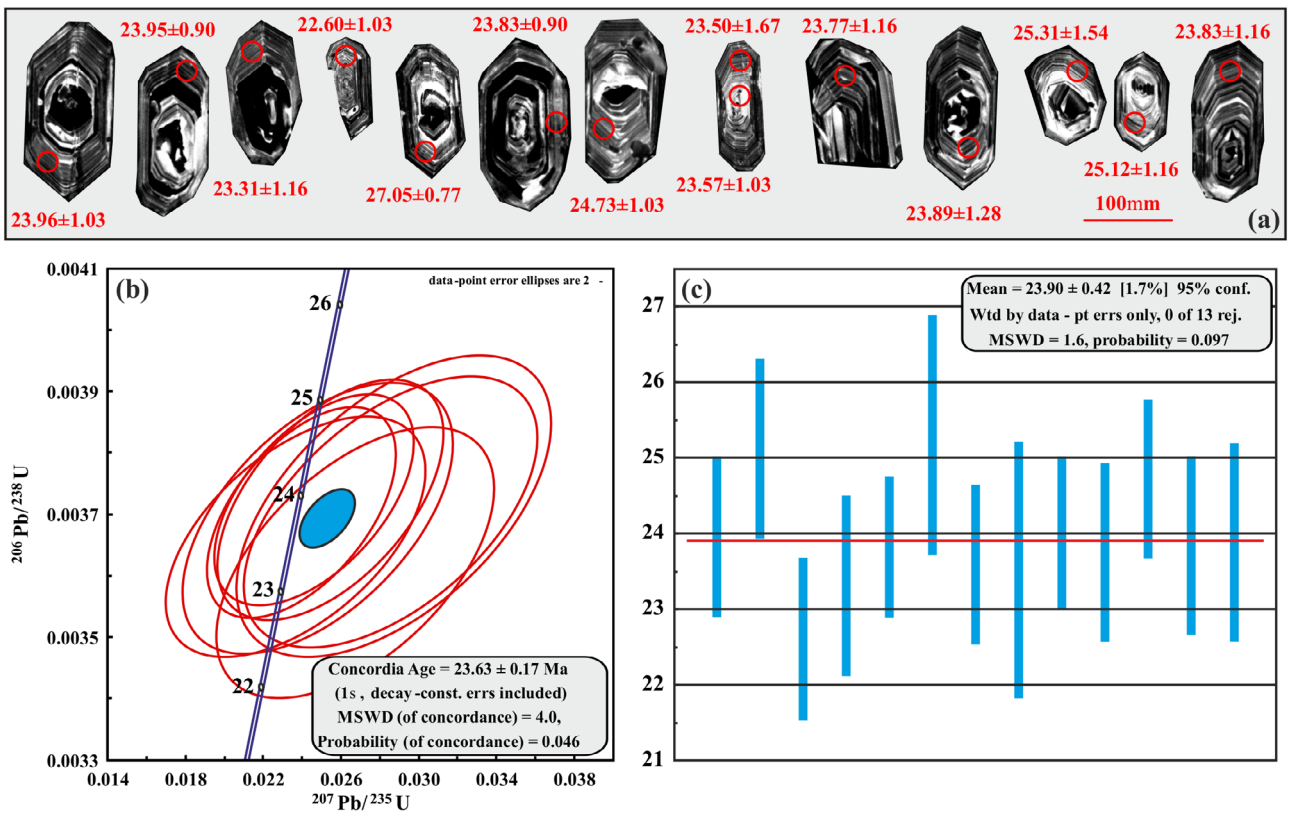

Figure 5. Zircon CL images with analysis points (spot sizes are 30 μm) a) concordia, b) weighted average, and c) diagrams for main plutonic body of Karadağ Pluton.

Table 1. Results of LA-ICP-MS U-Pb zircon ages of the main plutonic body of the Karadağ Pluton (c: core, r: rim).

Analysis points	$^{206}Pb/^{238}U$	1σ	$^{207}Pb/^{235}U$	1σ	$^{208}Pb/^{232}Th$	1σ	$^{207}Pb/^{206}Pb$	1σ	$^{206}Pb/^{238}U$	2σ	$^{207}Pb/^{235}U$	2σ	Th, ppm	U, ppm	Pb, ppm	Th/U
1r	0.00372	0.00008	0.0255	0.0024	0.0010	0.0001	0.0496	0.0047	23.96	1.03	25.54	4.69	590.2	1032.7	4.006	0.572
3rc	0.00390	0.00009	0.0306	0.0028	0.0012	0.0001	0.0568	0.0054	25.12	1.16	30.60	5.53	349.8	989.8	3.864	0.353
7cr	0.00351	0.00008	0.0275	0.0024	0.0010	0.0001	0.0568	0.0051	22.60	1.03	27.54	4.74	1572.4	1805.8	7.121	0.871
4cr	0.00362	0.00009	0.0267	0.0029	0.0009	0.0001	0.0535	0.0060	23.31	1.16	26.78	5.75	989.4	1204.1	4.707	0.822
8r	0.00420	0.00006	0.0395	0.0015	0.0014	0.0001	0.0682	0.0027	27.05	0.77	39.36	2.93	1338.1	3789.2	16.208	0.353
10r	0.00370	0.00007	0.0239	0.0020	0.0010	0.0001	0.0469	0.0040	23.83	0.90	24.03	3.94	908.0	1349.5	5.269	0.673
11r	0.00393	0.00012	0.0418	0.0044	0.0014	0.0001	0.0770	0.0085	25.31	1.54	41.56	8.64	445.1	818.6	3.517	0.544
14r	0.00366	0.00008	0.0237	0.0027	0.0009	0.0001	0.0469	0.0055	23.57	1.03	23.75	5.41	528.3	973.6	3.637	0.543
14c	0.00365	0.00013	0.0371	0.0050	0.0011	0.0001	0.0737	0.0103	23.50	1.67	37.01	9.82	501.6	697.3	2.832	0.719
16r	0.00372	0.00007	0.0246	0.0021	0.0009	0.0001	0.0479	0.0042	23.95	0.90	24.68	4.14	1027.6	1565.2	6.095	0.657
19r	0.00369	0.00009	0.0248	0.0028	0.0009	0.0001	0.0487	0.0057	23.77	1.16	24.87	5.62	547.2	972.4	3.671	0.563
22rc	0.00384	0.00008	0.0336	0.0026	0.0011	0.0001	0.0635	0.0050	24.73	1.03	33.60	5.08	480.7	775.3	3.188	0.620
26r	0.00370	0.00009	0.0286	0.0031	0.0010	0.0001	0.0559	0.0062	23.83	1.16	28.60	6.09	533.2	1094.6	4.153	0.487
25r	0.00371	0.00010	0.0287	0.0033	0.0009	0.0001	0.0561	0.0066	23.89	1.28	28.75	6.52	471.5	774.6	2.998	0.609

Table 2. K-Ar radiometric age determinations for the Karadağ Pluton (1: main plutonic body, 2: leucocratic facies).

Sample	Material	Weight (mg)	% K	% $^{40}Ar^*$	$^{40}Ar^*$ (pmol/g)	Age (Ma)	Error (Ma)
DG-5	Hornblende[1]	69.87	2.89	11.1	120.5	23.9	0.5
DG-7	Biotite[1]	73.36	3.92	11.0	139.0	20.3	0.3
DG-11	Hornblende[1]	77.34	3.10	9.3	109.0	20.2	0.9
DG-63	Whole-rock[2]	99.09	2.91	12.2	111.6	22.0	1.1

the BQF-diagram (Debon and Le Fort, 1988; Figure 6e). The Karadağ Pluton samples had high Al_2O_3 (12.25–16.35 wt.%), low TiO_2 (0.07–0.51 wt.%) and P_2O_5 (0.001–0.17 wt.%) contents, and variable concentrations of total Fe_2O_3 (0.6–5.66 wt.%). It had high alkali (Na_2O+K_2O) contents of 5.78–9.19 wt.%, and CaO contents that straddled from 0.61–5.51. It also had variable concentrations of MgO (0.08–4.72 wt.%, with Mg# ($Mg^{2+}/(Mg^{2+}+Fe^{2+})$) between 0.19 and 0.62. In addition, mafic index (Fe+Mg) ratios ranging from 0.006 to 0.153 and K/Na ratios ranging from 0.66 to 1.14 (Table 3) were defined.

In the normal mid-ocean ridge basalt (N-MORB) normalized trace elements diagram (Figure 7a), the Karadağ Pluton samples exhibited strong depletions in Ta, Nb, P, and high field strength elements (HFSEs) (Ti and Y), and significant enrichment in large ion lithophile elements (LILEs) (K, Rb, Ba, and Th). The decrease from Th to Ta and Nb was more profound than the decrease from La to Nd. In addition, Nd, Hf, Zr, and Sm formed an almost horizontal trend for the majority of the samples, except for a couple of samples that displayed elevated SiO_2 contents. In the chondrite-normalized REE diagram (Figure 7b), the samples were enriched in light REEs (LREEs) and depleted in heavy REEs (HREEs), and showed variable depletion of Eu ($Eu/Eu^* = 0.38–1.09$). As shown in the tectonic discrimination diagrams (Pearce et al., 1984; Gorton and Schandl, 2000), the samples of the Karadağ Pluton were plotted into volcanic arc granite (VAG) and syn-collision (syn-COLG) fields (Figure 8a), except for 1 sample that was plotted at the intersection of the plate setting with VAG-syn-COLG (Pearce et al., 1984). Moreover, these samples were plotted within the active continental margin (ACM) and oceanic arc fields in the Ta/Yb vs. Th/Yb diagram (Figure 8b) of Gorton and Schandl (2000). The high Th/Yb and Ba/La values of the samples (Figure 8c) can be used to identify the addition of slab-derived fluids and sediment-derived melts. In this diagram, the Karadağ Pluton samples showed variable Ba/La coupled with high Th/Yb values. The Ba/La ratios of the Karadağ Pluton samples were consistent with the addition of fluid from the subducted slab into the source region in the mantle (Hawkesworth et al., 1991), while the Th/Yb ratios showed that sediment-derived melts were added, especially in the late-stage leucocratic facies.

4.3. Whole rock Sr-Nd isotopes

The results of the whole-rock Sr-Nd isotopic data of the Karadağ Pluton samples are shown in Table 4. All of the initial $^{87}Sr/^{86}Sr$ isotopic ratios and εNd(t) values were calculated on the basis of its U-Pb age (ca. 23 Ma). The results indicated that the initial $^{87}Sr/^{86}Sr_{(i)}$ values for the Karadağ Pluton ranged from 0.706906 to 0.707068, while their initial $^{143}Nd/^{144}Nd_{(i)}$ values varied between 0.512474 and 0.512469. Their $\varepsilon Nd_{(i)}$ values ranged between –2.7 and –2.9 (Figure 9), with mantle Nd model ages of T_{DM} of 1.06–1.08 Ga (after Liew and Hofmann, 1988).

4.4. Mineral chemistry

4.4.1. Biotite

The chemical compositions of the biotites and calculated end members (based on 22 cation charges) are given in Table 5. A total of 28 spots were analyzed on selective biotite minerals from the Karadağ Pluton samples and plotted in the Mg-Al^{VI}+Fe^{3+}+Ti-Fe^{2+}+Mn classification diagram of Foster (1960), and it was found that all of the analyzed biotite minerals were classified as Mg-biotite (Figure 10a). In the Fe^{3+}–Fe^{2+}–Mg classification diagram (Figure 10b) of Wones (1989), which was used to determine the oxidation state of the biotite, all of the biotite minerals fell into the Ni-NiO (NNO) buffer field. The Ti-in biotite temperatures for the Karadağ Pluton samples were calculated using the Ti and X_{Mg} (Mg/(Mg+Fe) values of the analyzed biotite, as suggested by Henry et al. (2005). The calculated temperatures for the Karadağ Pluton samples ranged from 624 to 760 °C (mean: 720 ± 33 °C, Figure 10c). In the ΣFeO/(ΣFeO + MgO) vs. MgO (wt.%) binary diagram of Zhou (1986), the biotite minerals from the Karadağ Pluton samples were plotted within the crust-mantle mixed source and crust-derived source fields (Figure 10d).

4.4.2. Amphibole

The chemical composition of the amphiboles and calculated end members (based on 23 oxygen) are given in Table 6. A total of 22 spots were analyzed on selective amphibole minerals from the Karadağ Pluton and plotted in the $Mg/(Mg+Fe^{2+})$ vs. Si classification diagram of Leake et al.

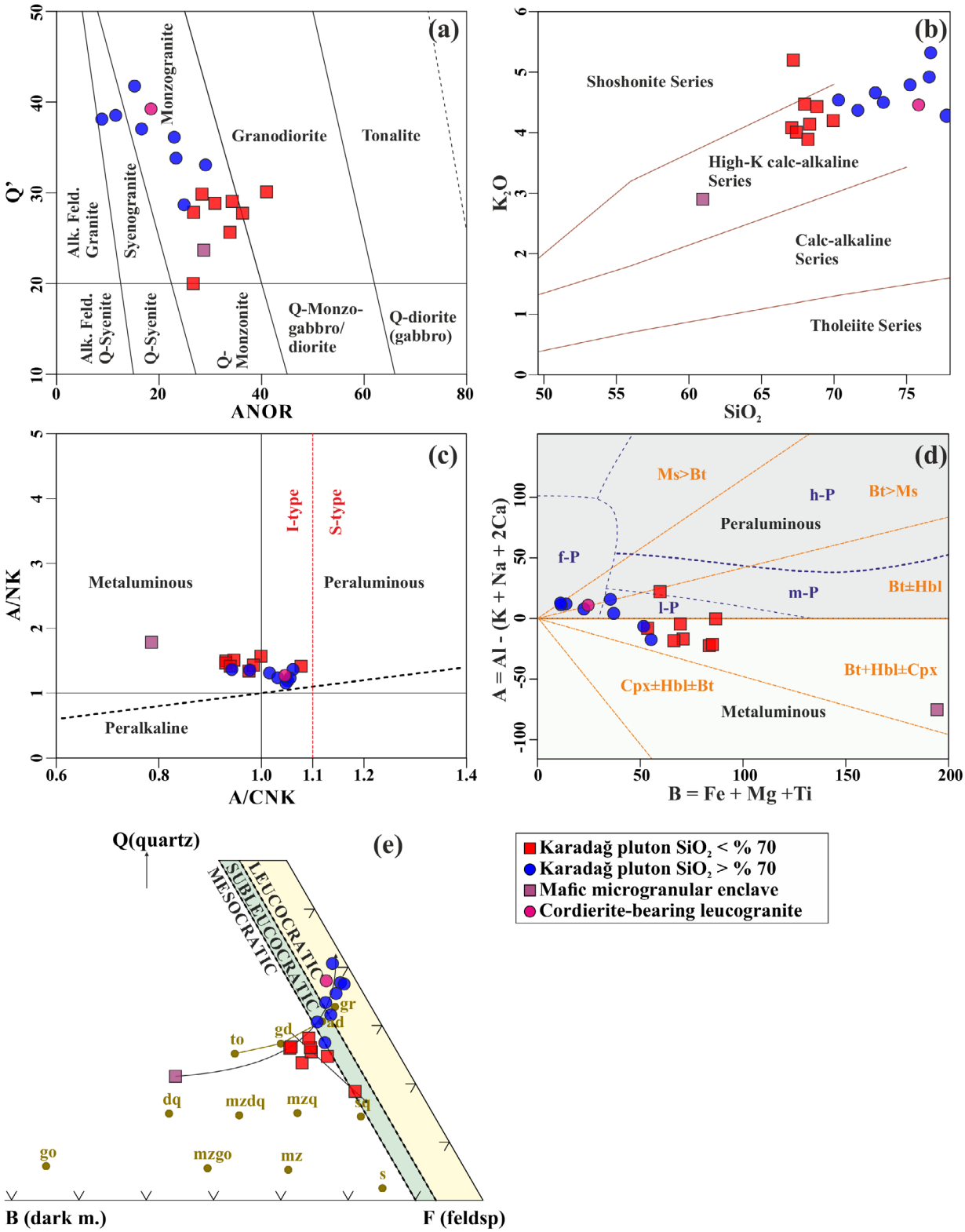

Figure 6. Classification diagrams of the Karadağ Pluton based on the a) Q'-ANOR diagram (Streckeisen and Le Maitre, 1979), b) SiO_2 vs K_2O diagram (Peccerillo and Taylor, 1976), c) A/CNK vs A/NK diagram of Shand (1943), d) B–A diagram (Debon and Le Fort, 1983; orange lines and words) modified by Villaseca et al. (1998), and e) Q-B-F diagram of Debon and Le Fort (1988).

Table 3. Whole-rock major oxides (wt.%), molar major elements (wt.%) trace and REEs (ppm) data from the Karadağ Pluton (*: cordierite-bearing leucogranite).

	Main plutonic body									Leucocratic facies								
Sample	DG-10	DG-45	DG-13	DG-6	DG-72B	DG-4	DG-5	DG-7	DG-11	DG-8	DG-14	DG-34B	DG-23	DG-34A	DG-63*	DG-34C	DG-72A	DG-12
SiO_2	60.95	67.09	67.19	67.41	67.97	68.2	68.32	68.82	69.94	70.31	71.64	72.85	73.4	75.24	75.83	76.56	76.66	77.75
TiO_2	0.51	0.41	0.34	0.39	0.35	0.36	0.43	0.36	0.33	0.3	0.29	0.21	0.2	0.16	0.12	0.11	0.07	0.08
Al_2O_3	14.06	15.28	16.35	15.42	15.67	15.22	14.61	14.98	14.42	14.53	13.93	13.86	13.9	13.04	12.8	12.62	12.49	12.25
Fe_2O_3	5.66	3.48	2.69	3.57	2.57	2.94	3.61	3.01	2.85	2.37	2.37	1.78	1.7	1.09	1.35	0.66	0.69	0.6
MnO	0.15	0.05	0.06	0.06	0.06	0.07	0.07	0.07	0.07	0.06	0.06	0.05	0.02	0.03	0.03	0.02	0.01	0.02
MgO	4.72	1.53	0.63	1.37	0.93	1.19	1.39	1.1	1.07	0.88	0.74	0.49	0.47	0.28	0.25	0.17	0.08	0.11
CaO	5.51	3.06	2.51	3.45	1.91	3.3	3.16	2.61	2.84	2.63	2.19	1.69	1.6	1.16	1.2	0.76	0.61	0.92
Na_2O	2.88	3.23	3.99	3.62	3.79	3.57	3.33	3.45	3.43	3.48	3.37	3.36	3.23	3.25	3.18	3.22	3.07	3.22
K_2O	2.9	4.08	5.2	4.01	4.47	3.89	4.14	4.43	4.2	4.54	4.37	4.66	4.5	4.79	4.46	4.92	5.32	4.28
P_2O_5	0.156	0.168	0.091	0.153	0.11	0.134	0.14	0.119	0.112	0.111	0.12	0.064	0.058	0.043	0.024	0.007	0.001	0.013
Cr_2O_3	0.035	0.002	0.002	0.002	0.002	0.002	0.002	0.003	0.002	0.002	0.003	0.003	0.002	0.002	0.002	0.002	0.002	0.002
LOI	2.1	1.3	0.6	0.3	2	0.9	0.6	0.8	0.5	0.6	0.7	0.8	0.8	0.8	0.7	0.9	1	0.7
Total	99.63	99.68	99.65	99.76	99.83	99.78	99.80	99.75	99.76	99.81	99.78	99.82	99.88	99.89	99.95	99.95	100.00	99.95
Si	1.014	1.117	1.118	1.122	1.131	1.135	1.137	1.145	1.164	1.170	1.192	1.212	1.222	1.252	1.262	1.274	1.276	1.294
Ti	0.006	0.005	0.004	0.005	0.004	0.005	0.005	0.005	0.004	0.004	0.004	0.003	0.003	0.002	0.002	0.001	0.001	0.001
Al	0.138	0.150	0.160	0.151	0.154	0.149	0.143	0.147	0.141	0.143	0.137	0.136	0.136	0.128	0.126	0.124	0.122	0.120
Fe	0.035	0.022	0.017	0.022	0.016	0.018	0.023	0.019	0.018	0.015	0.015	0.011	0.011	0.007	0.008	0.004	0.004	0.004
Mn	0.002	0.001	0.001	0.001	0.001	0.001	0.001	0.001	0.001	0.001	0.001	0.001	0.000	0.000	0.000	0.000	0.000	0.000
Mg	0.117	0.038	0.016	0.034	0.023	0.030	0.034	0.027	0.027	0.022	0.018	0.012	0.012	0.007	0.006	0.004	0.002	0.003
Ca	0.098	0.055	0.045	0.062	0.034	0.059	0.056	0.047	0.051	0.047	0.039	0.030	0.029	0.021	0.021	0.014	0.011	0.016
Na	0.046	0.052	0.064	0.058	0.061	0.058	0.054	0.056	0.055	0.056	0.054	0.054	0.052	0.052	0.051	0.052	0.050	0.052
K	0.031	0.043	0.055	0.043	0.047	0.041	0.044	0.047	0.045	0.048	0.046	0.049	0.048	0.051	0.047	0.052	0.056	0.045
P	0.001	0.001	0.001	0.001	0.001	0.001	0.001	0.001	0.001	0.001	0.001	0.000	0.000	0.000	0.000	0.000	0.000	0.000
Mafic index	0.15	0.06	0.03	0.06	0.04	0.05	0.06	0.05	0.04	0.04	0.03	0.02	0.02	0.01	0.01	0.01	0.01	0.01
A/CNK	0.79	1.00	0.98	0.93	1.08	0.95	0.93	0.98	0.94	0.94	0.98	1.02	1.06	1.03	1.05	1.05	1.05	1.06
Eu/Eu*	0.79	0.86	0.90	0.80	0.79	0.80	0.72	0.77	0.72	0.81	0.72	0.65	0.74	0.63	0.69	0.38	1.09	0.70
K/Na	0.66	0.83	0.86	0.73	0.78	0.72	0.82	0.84	0.81	0.86	0.85	0.91	0.92	0.97	0.92	1.01	1.14	0.87
Mg#	0.62	0.47	0.32	0.43	0.42	0.45	0.43	0.42	0.43	0.42	0.38	0.35	0.35	0.34	0.27	0.34	0.19	0.27
Ni	8.4	3.8	1.5	2.8	6.6	2.7	2.9	3.1	3.1	2.1	2.2	2.1	1.4	0.9	1	0.7	0.8	1.1
Sr	505.5	559	550.5	568.8	445.5	524	435.5	434.1	432.3	417.8	370.4	255.8	229.9	152.6	126.9	62.5	50.3	80.3
Ba	1005	1064	1716	922	879	1028	702	1040	934	726	944	811	334	479	115	115	91	102
Rb	121.8	192.1	215.3	178.4	191.6	149.9	168.3	222.7	179.7	199.3	196.1	284.9	245.1	282.2	264.6	295.5	262.7	187.1
Co	26.5	10.8	3.3	7.2	6.2	5.7	7.6	6.4	6.3	4.4	4.2	2.6	2.1	1.5	1.5	0.8	0.6	0.7
Cs	2.3	7.7	6.3	4.9	3.4	3.5	6	9.7	7.5	5.4	4.2	7.7	11.1	7.2	6.6	6.2	3.8	3.9
Ga	15.7	16.5	16.7	16.3	16.2	13.7	14.4	15.7	15.3	14.5	16.3	17	14.8	14.2	15.1	14.7	15.1	12.2

Table 3. (Continued.)

	Main plutonic body									Leucocratic facies								
Sample	DG-10	DG-45	DG-13	DG-6	DG-72B	DG-4	DG-5	DG-7	DG-11	DG-8	DG-14	DG-34B	DG-23	DG-34A	DG-63*	DG-34C	DG-72A	DG-12
Hf	4.0	3.3	6.9	4.4	4.8	3.9	4.6	5.3	3.7	5.0	4.1	5.3	3.5	4.2	3.4	3.3	3.0	2.0
Nb	10.8	14.9	25.9	14.7	16.3	13.7	16.7	16.5	14	16.1	17.5	17.9	16.5	14.9	18.6	29.3	24.3	13.9
Ta	0.9	1.5	2.1	1.4	1.3	1.3	1.6	1.5	1.4	1.4	1.8	1.7	1.8	1.4	1.3	3.4	2	0.9
Th	31.4	39.4	43.1	32.7	49.6	38.6	42.1	41.8	47.7	39.1	44.4	44.5	42.4	39.5	49.1	38.4	29.1	39.7
U	6.4	12.9	13.6	9.3	9.5	10.5	10.3	12.9	12	14.5	10.8	14.7	16.3	16.3	29.7	43.3	15.7	13.6
V	116	63	34	73	40	52	63	55	47	46	35	19	22	10	40	8	8	8
Zr	131.6	114.2	266.7	155.9	174.8	128.1	149.8	172.8	134.2	138.7	142.9	137.9	97.7	110.1	64.1	78.2	44.8	58.4
Y	18.4	15.4	17.3	18.2	15.8	15.1	17.1	16.1	15.9	13.9	16.3	15.3	9.6	9.4	7.7	9.1	1.9	9.1
La	37.6	42.8	40.8	49	34.8	41.2	49.3	50.8	73.1	43.4	44.1	50.2	45.5	42.9	30.5	42.3	18.2	40.4
Ce	69	75.9	84.1	87.5	53.7	67.5	79.9	86.1	108.3	70.8	76.4	84.4	69	65.8	43.4	61	19.3	48.1
Pr	7.85	8.04	8.98	9.44	7.07	8.4	9.91	8.72	10.06	7.22	7.9	8.25	6.25	6.08	3.95	5.33	1.3	4.14
Nd	28.4	26.9	28.4	31.2	24.3	27	30	27	30.8	24	25.9	25.8	18	16.6	10.3	14.2	2.7	10.2
Sm	5.06	4.08	4.02	4.87	3.87	4.59	5.17	4.21	4.33	3.6	4	3.64	2.29	2.21	1.35	1.73	0.35	1.16
Eu	1.17	1.02	1.01	1.1	0.92	1.08	1.09	0.91	0.87	0.82	0.8	0.66	0.47	0.4	0.28	0.18	0.11	0.23
Gd	4.02	3.2	2.94	3.67	3.26	3.7	4.12	3.14	3.17	2.68	2.92	2.66	1.66	1.69	1.13	1.22	0.27	1.01
Tb	0.61	0.5	0.47	0.57	0.46	0.54	0.62	0.49	0.5	0.42	0.46	0.41	0.27	0.25	0.17	0.2	0.04	0.17
Dy	3.15	2.47	2.71	2.86	2.66	3.04	3.44	2.59	2.59	2.06	2.6	2.16	1.42	1.42	0.99	1.08	0.27	0.93
Ho	0.59	0.5	0.54	0.58	0.57	0.56	0.64	0.51	0.49	0.43	0.48	0.45	0.28	0.28	0.24	0.25	0.05	0.22
Er	1.85	1.45	1.64	1.7	1.57	1.63	1.92	1.62	1.51	1.28	1.44	1.45	0.91	0.93	0.76	0.83	0.22	0.88
Tm	0.29	0.22	0.29	0.28	0.25	0.25	0.31	0.25	0.23	0.21	0.24	0.24	0.17	0.17	0.16	0.16	0.04	0.16
Yb	1.76	1.5	2.07	1.82	1.72	1.58	2.05	1.73	1.6	1.46	1.65	1.64	1.21	1.09	1.1	1.38	0.39	1.24
Lu	0.28	0.25	0.36	0.3	0.29	0.26	0.32	0.31	0.27	0.26	0.29	0.29	0.22	0.22	0.23	0.26	0.1	0.24

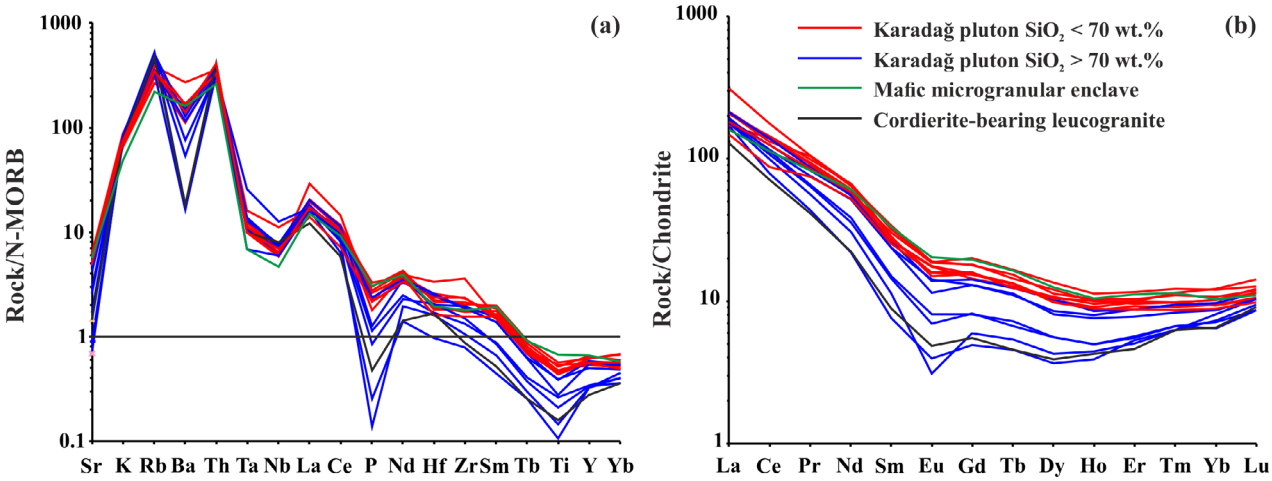

Figure 7. a) N-type MORB (Sun and McDonough, 1989) normalized spidergram and b) chondrite normalized (Sun and McDonough, 1989) spidergram for the Karadağ Pluton.

(1997), wherein the analyzed amphiboles were classified as magnesiohornblende (^{T}Si > 6.5 apfu) and tschermakite (^{T}Si < 6.5 apfu) (Figure 11a). The amphibole minerals of the Karadağ Pluton samples were in the calcic (^{B}Ca >1 apfu) subgroup, based on the International Mineralogical Association classification and Fe^{3+} calculation proposed by Leake et al. (1997). In the $Ca+Al^{IV}$ (3.06–3.38 apfu) vs. Si+Na+K (6.98–7.60 apfu) diagram of Giret et al. (1980), the studied amphiboles fell into the primary magmatic-originated hornblende and edenitic hornblende fields (Figure 11b). The amphibole crystallization temperatures for the Karadağ Pluton samples were in the range of 834 to 896 °C, with an average of 867 ± 22 °C, and the barometries varied between 1.45 and 2.12 kbar, with an average of 1.71 ± 0.23 kbar (Table 7). The estimated crystallization depths of the amphiboles were between 5.5 and 8 km (mean: 6.5 km). The oxygen fugacity of the studied amphiboles ($\log fO_2$) was between −10.16 and −12.53 bar (mean: −11.62 ± 0.4 bar) and all of the samples were plotted in the NNO and NNO+2 fields in the T–$\log fO_2$ diagram (Figure 11c). The H_2O_{melt} contents were between 3.44% and 6.32% (mean: 4.96 ± 0.4%), and the majority of the samples were situated between the maximum thermal stability and upper limit of the consistent amphibole curves in the H_2O_{melt}–T diagram (Figure 11d; Ridolfi et al., 2010). In the P-T diagram (Ridolfi et al., 2010), the amphibole minerals of the Karadağ Pluton samples were plotted between the maximum thermal stability and upper limit of the consistent amphibole curves and belonged to domain 1 (Mg–Hbl+Pl±Opx±Mgn±Ilm±Bt) and domain 2 (Tsc-Prg+Pl±Cpx± Opx±Mgn±Ilm) (Figure 11e).

5. Discussion

5.1. Crystallization conditions

The calculated biotite crystallization temperatures of the Karadağ Pluton samples varied between 624 and 760 °C (mean: 720 ± 33 °C, Figure 10d). The calculated amphibole temperatures for the Karadağ Pluton samples were in the range of 834–896 °C (mean: 867 ± 22 °C), and these calculated values (Figures 11c, 11d, and 11e) were consistent with amphibole-bearing calc-alkaline magma generation (Ridolfi at al., 2010; Ridolfi and Renzulli 2012, Putirka, 2016). The calculated amphibole barometries (Ridolfi et al., 2010) were in the range of 1.45 to 2.12 kbar, and based on the barometric calculations, the estimated depth of the amphibole crystallization was in the range of 5.5–8 km, which indicated that the amphiboles of the Karadağ Pluton crystallized at shallow crustal levels. The calculated pressure and temperature values of the Karadağ Pluton were compatible with all other Oligo-Miocene plutons in western Anatolia (Aysal, 2015 and references therein). Based on the amphibole and biotite mineral chemistry data, the oxygen fugacity of the Karadağ Pluton showed a relatively high oxidation state (ΔNNO: 0.19–2.19), that had equilibrated at a relatively high oxygen fugacity, similar to other Oligo-Miocene plutons in NW Anatolian. The H_2O_{melt} contents were between 3.44% and 6.32% (mean: 4.96 ± 0.4 %), and the majority of the samples were situated between the maximum thermal stability and upper limit of the consistent amphibole curves in the H_2O_{melt}–T diagram (Ridolfi et al., 2010). In the P-T diagram (Ridolfi et al., 2010), the amphibole minerals of the Karadağ Pluton samples were plotted between the maximum thermal stability

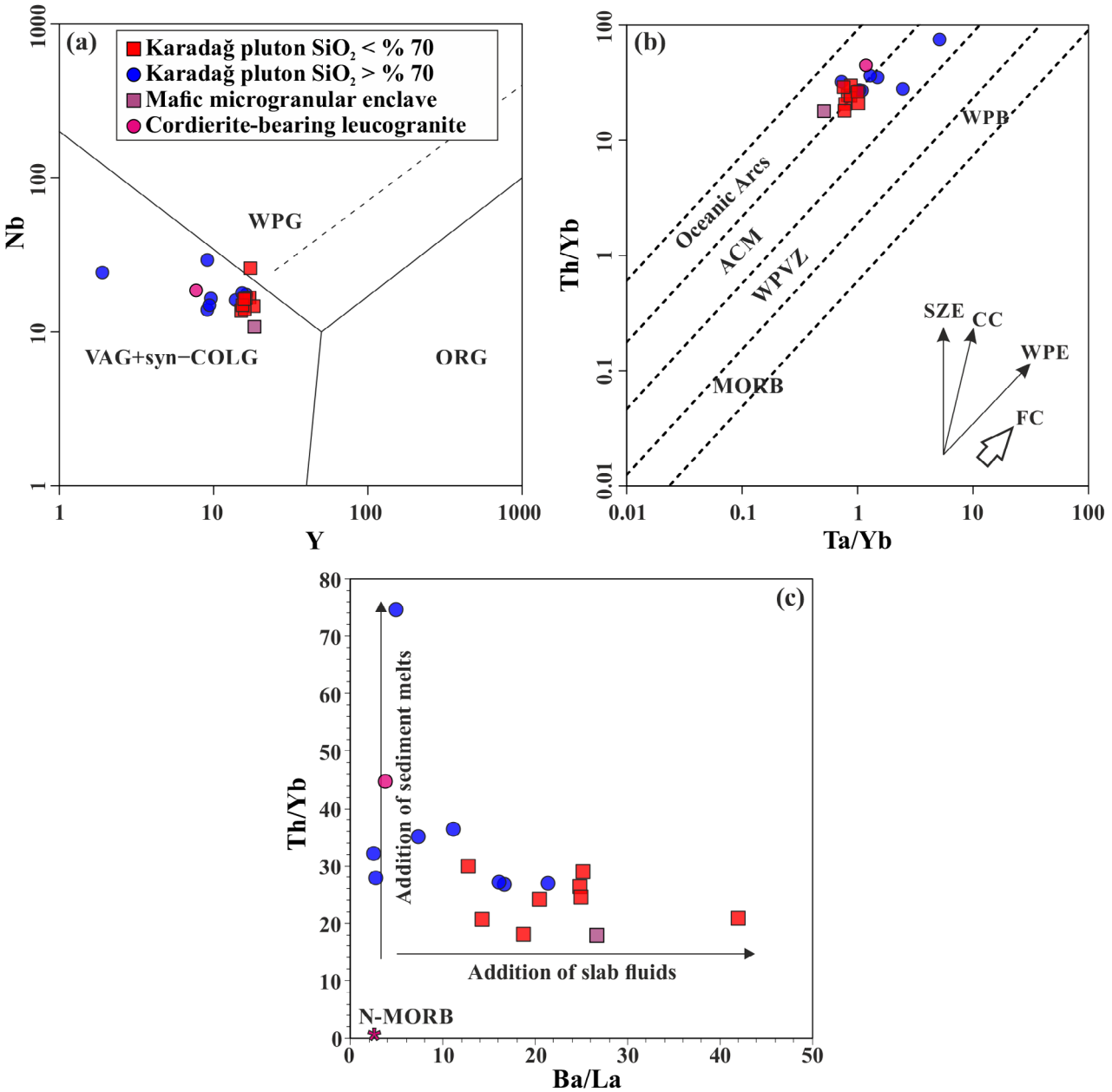

Figure 8. Tectonic discrimination diagrams for the Karadağ Pluton: a) Binary plot Y vs. Nb (Pearce et al., 1984), b) Ta/Yb vs. Th/Yb diagram (Gorton and Schandl, 2000), and c) Ba/La vs. Th/Yb diagram.

Table 4. Sr and Nd isotopic compositions of the Karadağ Pluton (*: cordierite-bearing leucogranite).

Sample	Age	Sr	Rb	Sm	Nd	$^{87}Rb/^{86}Sr$	$^{87}/^{86}Sr$	$^{87}/^{86}Sr_{(i)}$	$^{147}Sm/^{144}Nd$	$^{143}/^{144}Nd$	$^{143}/^{144}Nd_{(i)}$	$eNd_{(i)}$	TDM (Ga)
DG-7	23	434	223	4.210	27.00	1.4843	0.707553	0.707068	0.0947	0.512474	0.512460	–2.9	1.08
DG-11	23	432	180	4.33	30.8	1.2026	0.707347	0.706954	0.0854	0.512479	0.512466	–2.8	1.07
DG-63*	23	127	265	1.35	10.3	6.0334	0.708877	0.706906	0.0796	0.512481	0.512469	–2.7	1.06

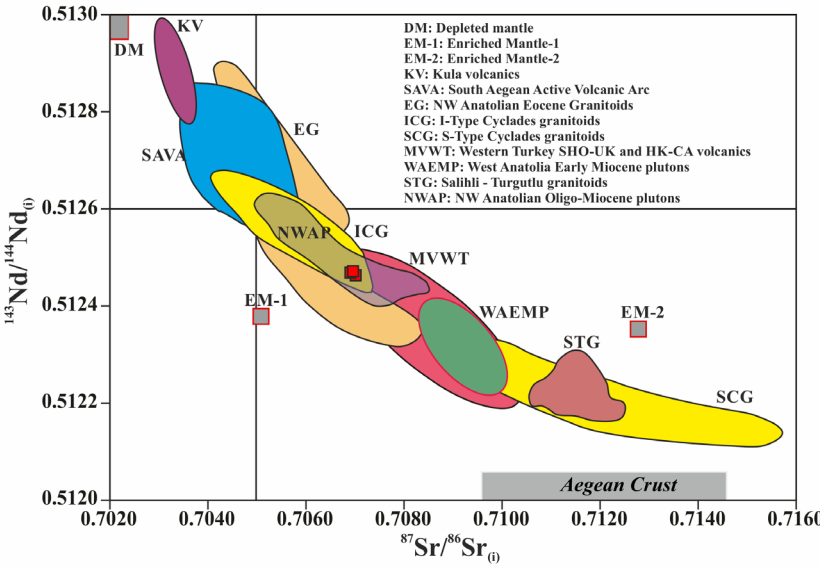

Figure 9. $^{87}Sr/^{86}Sr_{(i)}$ vs $^{143}Nd/^{144}Nd_{(i)}$ diagram for the Karadağ Pluton, and correlation with the other NW Anatolian plutons and Aegean regions (adopted from Aysal 2015 and references therein). The fields of different reservoirs and magmatic fields were also underlined by Aysal (2015).

and upper limit of the consistent amphibole curves, and belonged to domain 1 (Mg–Hbl+Pl±Opx±Mgn±Ilm±Bt) and domain 2 (Tsc-Prg+Pl±Cpx± Opx±Mgn±Ilm) (Figure 11e). These calculated values were compatible with those of calc-alkali magmas formed in an arc setting, and the Karadağ Pluton was emplaced and cooled in a shallow level magma chamber and at physicochemical conditions that were similar to the other Oligocene-Miocene plutons in the Biga Peninsula.

5.2. Petrogenesis

Magma evolution processes, such as partial melting, FC, magma mingling-mixing, and assimilation, are very important for understanding the source of the magma, ascent, and emplacement history. All of these processes related to the Karadağ Pluton are discussed in detail below.

5.2.1. FC and AFC processes

Harker variation diagrams provided useful information for monitoring the evolutionary trend of igneous rocks. In major and trace element Harker variation diagrams (Figure 12), for the majority of the samples from the Karadağ Pluton, the Ti, Fe, Mg, Ca, and P showed positive correlation with the increasing mafic index (Fe+Mg), wherein Si and K showed negative correlation, and Al and Na showed 2 different trends, comprising both an increase and decrease with the increasing mafic index. In fact, this followed a weak trend in the Si and K. However, V, Sr, Y, Ce, Zr, and Eu/Eu* showed positive correlation with the mafic index, except for the MME sample. While this behavior was generally compatible with FC processes, contrary to some samples, it showed that magmas derived from 2 different sources (mantle- and crust-derived) may have been mixed. In addition, the positive correlations between Ti, Al, Fe, Mg, Ca, V, Sr, and Y, and the increasing mafic index indicated the fractionation of mafic minerals, such as clinopyroxene, hornblende, biotite, and Ca-rich plagioclase. Moreover, accessory mineral phases, such as titanite and ilmenite fractionation, were represented by the positive correlation between Ti and the mafic index.

FC processes were investigated using the FC-Modeler (Keskin, 2002) excel spread sheet program with the Kd values of the intermediate magmas for the selected minerals. In the Sr-Ba, Rb-Ba and Rb-Sr plots (Figures 13a–13c), plagioclase, orthoclase, biotite, and hornblende crystallization trends could be clearly identified. In the Rb/V vs. Rb and Rb/V vs. 1/V diagrams (Figures 13d and 13e), the majority of the samples were consistent with FC or magma mixing trends. In the SiO_2 vs. $^{87}Sr/^{86}Sr$ and εNd diagrams (Figures 13f and 13g), all of the samples were plotted together with the compilation of the Sr-Nd isotopes of the Oligo-Miocene plutons (Aysal, 2015 and references therein), and the Sr-Nd isotope composition of the Karadağ Pluton was consistent with the FC trend. When the samples

Table 5. Representative chemical composition (wt.%) and structural formula of biotites of the Karadağ Pluton.

Sample No.	DG-45	DG-45	DG-45	DG-45	DG-45	DG-45	DG-45	DG-45	DG-45	DG-45	DG-4	DG-4	DG-4	DG-4	DG-4	DG-6	DG-6	DG-6	DG-6	DG-6	DG-6	DG-6	DG-6	DG-6	DG-6	DG-6	DG-6	DG-6
Point No.	1	2	3	4	5	6	7	8	9	10	1	2	3	4	5	1	2	3	4	5	6	7	8	9	10	11	12	13
SiO_2	36.82	36.21	35.35	35.01	34.61	34.43	34.31	33.81	33.8	33.44	33.09	32.43	35.5	35.02	34.8	35.15	34.7	34.9	35.22	35.02	35.8	35.24	35.99	34.81	34.37	35.24	36.55	34.71
TiO_2	4.28	4.23	4.52	3.18	3.65	2.69	4.04	3.59	4.14	4.14	2.45	3.93	4.86	4.84	4.75	4.85	4.36	4.69	4.51	4.77	4.33	4.82	4.67	4.85	4.88	4.15	4.01	4.22
Al_2O_3	13.45	13.31	13.69	13.59	13.68	13.68	13.88	13.57	13.5	13.38	14.41	12.96	14.38	14.85	14.9	15.15	14.92	15.36	15.38	15.64	14.96	15.27	14.9	15.23	15.3	15.52	15.11	16.15
FeOt	17.39	17.64	16.1	18.23	17.92	17.92	17.61	16.43	15.67	16.2	18.68	16.35	12.69	12.92	13.07	14	14.86	14.64	15.34	15.15	14.75	13.76	13.68	14.06	14.06	15.27	14.52	15.74
MnO	0.27	0.29	0.25	0.18	0.36	0.29	0.26	0.29	0.37	0.24	0.39	0.32	0.38	0.35	0.35	0.22	0.23	0.22	0.22	0.21	0.22	0.34	0.34	0.34	0.34	0.27	0.26	0.29
MgO	12.88	12.63	13.15	12.8	13.58	13.88	11.86	13.67	12.58	13.41	13.08	12.96	16.86	16.95	17.07	15.6	15.06	15.25	15.2	15.14	14.59	16.75	16.64	16.88	17.02	15.15	15.2	14.86
CaO	0.02	0.01	0.05	0.01	0.02	0.09	0.05	0.03	0.06	0.01	0.03	0.09	0.08	0	0	0.12	0.65	0.1	0.09	0.02	1.11	0.04	1.2	0.02	0.11	0.15	0.42	0.12
Na_2O	0.2	0.22	0.18	0.14	0.15	0.13	0.16	0.15	0.16	0.13	0.14	0.18	0.19	0.13	0.13	0.22	0.22	0.17	0.28	0.16	0.98	0.14	0.12	0.15	0.13	0.36	0.92	0.31
K_2O	9.25	8.94	8.26	7.51	7.9	7.5	7.81	8.06	7.91	7.92	6.52	7.98	10.28	10.31	10.3	9.73	9.74	9.88	9.07	9.22	8.22	8.22	8.99	9.08	9.09	9.07	8.53	8.52
H_2O^*	5.40	5.33	5.25	5.18	5.17	5.18	5.14	5.12	5.06	5.08	5.07	4.96	4.75	4.56	4.55	5.06	5.01	5.05	5.07	5.07	5.06	5.10	5.02	5.09	5.07	5.06	5.11	5.05
Total	99.96	98.81	96.80	95.83	97.04	95.79	95.12	94.72	93.25	93.95	93.86	92.16	99.97	99.93	99.92	100.10	99.75	100.26	100.38	100.40	100.02	99.68	101.55	100.51	100.37	100.24	100.63	99.97
Si	2.81	2.80	2.77	2.79	2.73	2.74	2.75	2.72	2.75	2.71	2.69	2.70	2.66	2.63	2.61	2.65	2.64	2.63	2.65	2.63	2.69	2.64	2.66	2.61	2.58	2.65	2.72	2.62
Al^{IV}	1.19	1.20	1.23	1.21	1.27	1.26	1.25	1.28	1.25	1.28	1.31	1.27	1.27	1.31	1.32	1.35	1.34	1.37	1.35	1.37	1.31	1.35	1.30	1.34	1.35	1.35	1.28	1.38
ΣT	4	4	4	4	4	4	4	4	4	4	4	4	4	4	4	4	4	4	4	4	4	4	4	4	4	4	4	4
Al^{VI}	0.03	0.02	0.03	0.06	0.00	0.03	0.07	0.01	0.05	0.00	0.08	0.00	0.00	0.00	0.00	0.00	0.00	0.00	0.01	0.02	0.02	0.00	0.00	0.00	0.00	0.03	0.05	0.06
Ti	0.25	0.25	0.27	0.19	0.22	0.16	0.24	0.22	0.25	0.25	0.15	0.25	0.27	0.27	0.27	0.28	0.25	0.27	0.26	0.27	0.25	0.27	0.26	0.27	0.28	0.24	0.23	0.24
Fe^{3+}	0.34	0.39	0.51	0.55	0.69	0.64	0.52	0.62	0.52	0.69	0.79	0.67	0.57	0.64	0.67	0.56	0.44	0.56	0.62	0.66	0.26	0.85	0.51	0.83	0.87	0.55	0.33	0.66
Fe^{2+}	0.77	0.75	0.55	0.66	0.50	0.55	0.66	0.48	0.55	0.41	0.48	0.47	0.23	0.17	0.15	0.32	0.50	0.36	0.35	0.29	0.66	0.02	0.34	0.05	0.01	0.41	0.58	0.34
$Fe^{3+}{}_{(T)}$	0.00	0.00	0.00	0.00	0.00	0.00	0.00	0.00	0.00	0.01	0.00	0.03	0.07	0.06	0.07	0.01	0.02	0.00	0.00	0.00	0.00	0.01	0.05	0.05	0.07	0.00	0.00	0.00
$Fe^{3+}{}_{(M)}$	0.34	0.39	0.51	0.55	0.68	0.64	0.52	0.62	0.52	0.68	0.79	0.64	0.50	0.58	0.60	0.56	0.42	0.56	0.62	0.66	0.26	0.83	0.46	0.78	0.81	0.55	0.33	0.66
Mn	0.02	0.02	0.02	0.01	0.02	0.02	0.02	0.02	0.03	0.02	0.03	0.02	0.02	0.02	0.02	0.01	0.02	0.01	0.01	0.01	0.01	0.02	0.02	0.02	0.02	0.02	0.02	0.02
Mg	1.47	1.46	1.54	1.52	1.60	1.65	1.42	1.64	1.53	1.62	1.59	1.61	1.89	1.90	1.91	1.75	1.71	1.72	1.70	1.70	1.64	1.87	1.83	1.88	1.90	1.70	1.69	1.67
Na	0.00	0.00	0.00	0.00	0.00	0.01	0.00	0.00	0.01	0.00	0.00	0.01	0.01	0.00	0.00	0.01	0.05	0.01	0.01	0.00	0.09	0.00	0.10	0.00	0.01	0.01	0.03	0.01
K	0.03	0.03	0.03	0.02	0.02	0.02	0.03	0.02	0.03	0.02	0.02	0.03	0.03	0.02	0.02	0.03	0.03	0.03	0.04	0.02	0.14	0.02	0.02	0.02	0.02	0.05	0.13	0.05
Ca	0.90	0.88	0.83	0.76	0.79	0.76	0.80	0.83	0.82	0.82	0.68	0.85	0.98	0.99	0.99	0.94	0.95	0.95	0.87	0.88	0.79	0.79	0.85	0.87	0.87	0.87	0.81	0.82
Total oxi.	95.58	94.32	92.14	91.15	92.25	90.94	90.28	89.75	88.34	88.92	88.74	86.96	95.86	95.87	95.81	95.58	95.15	95.67	95.87	95.83	95.68	95.14	97.31	95.86	95.61	95.74	96.46	95.33
Mg#	0.57	0.56	0.59	0.56	0.58	0.58	0.55	0.60	0.59	0.60	0.56	0.59	0.70	0.70	0.70	0.67	0.64	0.65	0.64	0.64	0.64	0.69	0.68	0.68	0.68	0.64	0.65	0.63
Fe#	0.43	0.44	0.41	0.44	0.43	0.42	0.45	0.40	0.41	0.40	0.45	0.41	0.30	0.30	0.30	0.34	0.36	0.35	0.36	0.36	0.36	0.32	0.32	0.32	0.32	0.36	0.35	0.37
Al_{tot}	1.21	1.21	1.26	1.27	1.27	1.29	1.31	1.29	1.30	1.28	1.38	1.27	1.27	1.31	1.32	1.35	1.34	1.37	1.36	1.39	1.33	1.35	1.30	1.34	1.35	1.38	1.33	1.44
I-site	0.93	0.92	0.86	0.79	0.82	0.79	0.83	0.85	0.85	0.84	0.70	0.88	1.02	1.01	1.01	0.98	1.03	0.98	0.92	0.91	1.02	0.81	0.96	0.89	0.90	0.94	0.98	0.88

Table 5. (Continued).

Sample No.	DG-45	DG-45	DG-45	DG-45	DG-45	DG-45	DG-45	DG-45	DG-45	DG-45	DG-4	DG-4	DG-4	DG-4	DG-4	DG-6	DG-6	DG-6	DG-6	DG-6	DG-6	DG-6	DG-6	DG-6	DG-6	DG-6	DG-6	DG-6
M-site	3.02	3.02	3.00	3.07	3.07	3.11	2.98	3.02	2.94	2.98	3.10	2.94	3.01	3.02	3.02	2.99	2.96	2.99	3.04	3.03	2.95	3.10	3.02	3.07	3.06	3.03	3.02	3.04
IMTA-sites	7.96	7.93	7.85	7.86	7.89	7.90	7.81	7.87	7.80	7.83	7.81	7.82	8.03	8.02	8.03	7.97	7.99	7.98	7.95	7.93	7.97	7.90	7.98	7.96	7.96	7.97	8.00	7.92
Ph	0.49	0.48	0.51	0.49	0.52	0.53	0.48	0.54	0.52	0.54	0.51	0.54	0.61	0.62	0.62	0.58	0.57	0.57	0.56	0.56	0.55	0.60	0.60	0.60	0.61	0.56	0.56	0.55
Ann	0.26	0.25	0.18	0.22	0.16	0.18	0.22	0.16	0.19	0.14	0.16	0.16	0.08	0.06	0.05	0.11	0.17	0.12	0.11	0.10	0.23	0.01	0.11	0.02	0.00	0.14	0.19	0.11
Pdo	0.16	0.17	0.20	0.21	0.24	0.22	0.19	0.22	0.18	0.23	0.25	0.21	0.22	0.23	0.24	0.22	0.17	0.21	0.23	0.24	0.13	0.30	0.20	0.29	0.29	0.21	0.15	0.24
Mnb	0.01	0.01	0.01	0.00	0.01	0.01	0.01	0.01	0.01	0.01	0.01	0.01	0.01	0.01	0.01	0.01	0.01	0.01	0.01	0.00	0.01	0.01	0.01	0.01	0.01	0.01	0.01	0.01
Alb	0.01	0.01	0.01	0.02	0.00	0.01	0.02	0.00	0.02	0.00	0.03	0.00	0.00	0.00	0.00	0.00	0.00	0.00	0.00	0.01	0.01	0.00	0.00	0.00	0.00	0.01	0.02	0.02
Tib	0.08	0.08	0.09	0.06	0.07	0.05	0.08	0.07	0.09	0.08	0.05	0.08	0.09	0.09	0.09	0.09	0.08	0.09	0.08	0.09	0.08	0.09	0.08	0.09	0.09	0.08	0.07	0.08
Phlogopite	29.09	21.54	0.00	0.00	0.00	0.00	0.00	0.00	0.00	0.00	0.00	0.00	0.00	0.00	0.00	3.65	21.27	6.49	0.00	0.00	44.69	0.00	6.33	0.00	0.00	6.22	37.35	0.00
Ti-phlogopite	24.60	24.63	26.52	18.12	18.01	14.38	23.88	19.92	25.22	20.60	10.97	20.88	27.42	25.24	23.98	27.47	24.96	26.62	24.10	23.89	24.50	18.56	25.93	19.39	18.82	23.51	22.47	21.16
Ferri-eastonite	33.96	39.02	50.93	55.27	68.52	64.35	51.95	62.31	51.72	68.80	78.77	66.94	56.66	64.17	67.14	56.31	44.33	55.99	61.87	65.85	26.41	84.51	50.50	83.37	87.27	54.77	32.48	65.82
Muscovite	5.66	6.50	8.46	8.77	9.80	9.56	8.48	9.52	8.58	0.23	9.60	2.35	5.97	5.45	6.01	0.23	9.45	9.33	9.74	9.72	4.40	0.58	3.11	3.58	4.57	9.13	5.41	9.69
Talc	6.69	8.30	14.28	20.49	15.12	18.69	16.76	13.44	14.73	13.02	21.81	9.90	0.00	0.00	0.00	2.34	0.00	1.57	7.70	8.05	0.00	13.08	4.13	7.81	6.97	6.37	2.28	11.00
T °C	708	706	725	666	699	644	701	697	717	718	624	712	760	759	756	748	729	740	731	739	726	752	750	753	754	720	718	719
Name	Mg-Bt	Mg-Bt	Mg-Bt	Mg-Bt	Mg-Bt	Mg-Bt	Mg-Bt	Mg-Bt	Mg-Bt	Mg-Bt	Mg-Bt	Mg-Bt	Mg-Bt	Mg-Bt	Mg-Bt	Mg-Bt	Mg-Bt	Mg-Bt	Mg-Bt	Mg-Bt	Mg-Bt	Mg-Bt	Mg-Bt	Mg-Bt	Mg-Bt	Mg-Bt	Mg-Bt	Mg-Bt	Mg-Bt

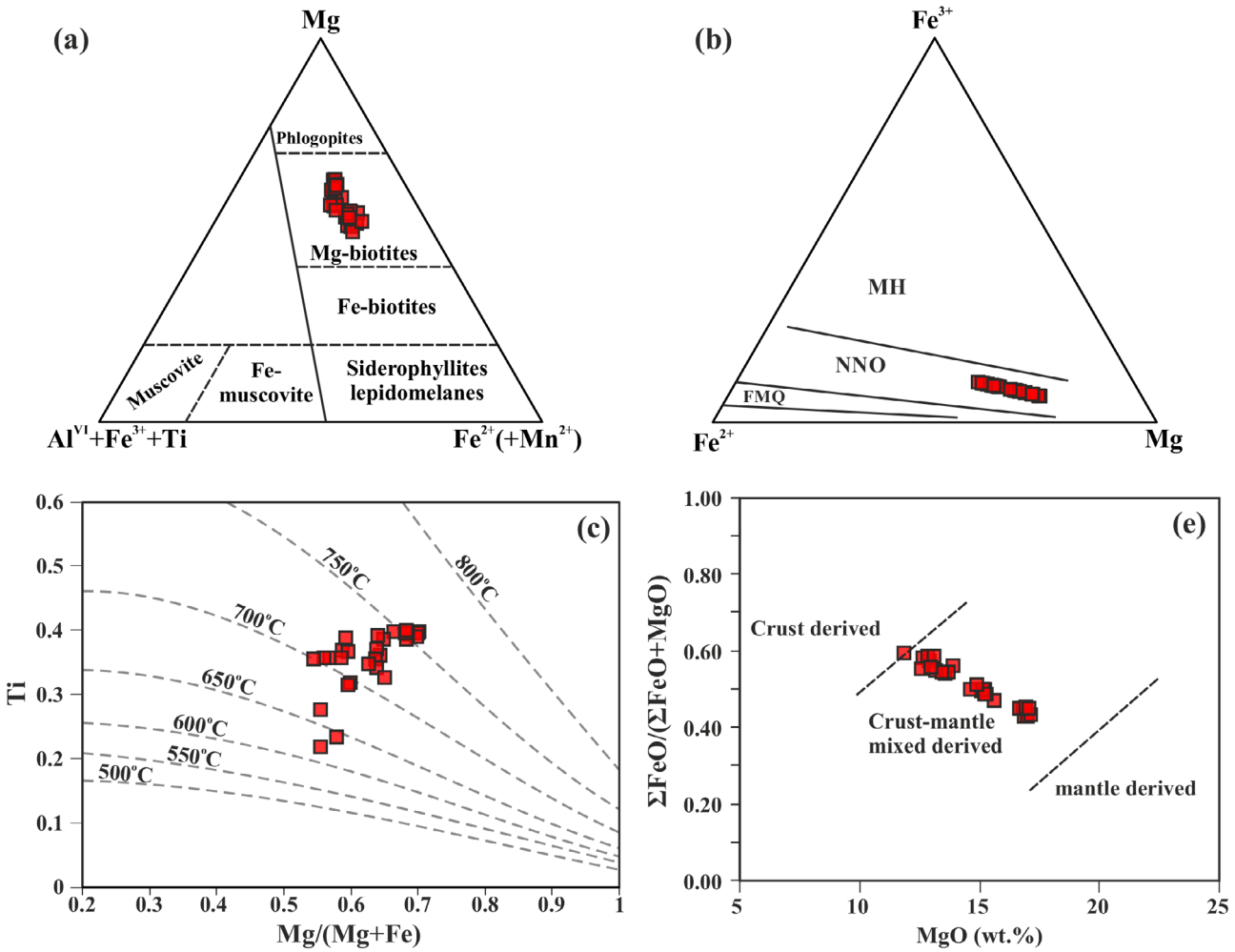

Figure 10. a) Mg–Al^{VI}+Fe^{3+}+Ti–Fe^{2+}+Mn classification diagram (Foster, 1960), b) Fe^{3+}–Fe^{2+}–Mg classification diagram (Wones, 1989), c) Ti vs Mg/(Mg+Fe) variation diagram of biotite (Henry et al., 2005), and d) ΣFeO)/(ΣFeO + MgO) vs. MgO (wt.%) binary diagram (Zhou, 1986).

were plotted on the normative diopside and corundum vs. SiO_2 diagram (Figure 13h), it can be seen that the corundum increased and the diopside gradually decreased with increasing SiO_2. However, considering that the ASI values of the Karadağ Pluton samples were less than 1.1, this indicated that the crustal assimilation was not so pervasive.

5.2.2. Magma mixing-mingling

Magma mixing-mingling is another important process for understanding the evolution history of plutonic rocks. Usually, evidence of magma mixing-mingling processes can be revealed by field studies, petrographic observations, as well as the geochemistry and Sr-Nd isotope ratios of the pluton. While magma mingling can be explained by the presence of the MMEs in the field, some textural and geochemical properties of the host pluton and its enclaves are also very important for the understanding of magma mixing. The Karadağ Pluton has MMEs and wall-rock xenoliths. The MMEs of the Karadağ Pluton have sharp contacts with the host pluton and have ellipsoidal shapes, varying in size from centimeters to meters (Figure 3). The MMEs have a microdioritic, quartzmicrodioritic, and monzodioritic composition, and they include more mafic minerals than intermediate and felsic granitic host rocks. Both the host rocks and the MMEs have some mixing textures, such as boxy- and spongy-cellular plagioclase, rapakivi and antirapakivi textured feldspars, poikilitic K-feldspar and plagioclase textures, blade-shaped biotite, acicular apatite, and quartz-biotite ocellar textures, as described in Hibbard (1991). Boxy and spongy-cellular plagioclase tex-

Table 6. Representative EPMA analyses results and calculated end-members of the amphibole minerals.

Sample No.	DG-45	DG-45	DG-45	DG-45	DG-45	DG-45	DG-45	DG-45	DG-45	DG-4	DG-4	DG-4	DG-4	DG-4	DG-4	DG-4	DG-4	DG-4	DG-6	DG-6	DG-6	DG-6
Point No.	1	2	3	4	5	6	7	8	9	1	2	3	4	5	6	7	8	9	1	2	3	4
SiO_2	45.47	45.40	46.39	46.14	45.92	45.25	44.50	45.77	45.69	45.69	45.36	45.00	46.02	45.19	45.51	45.70	45.31	45.63	45.60	45.83	45.90	45.09
TiO_2	2.53	2.28	2.45	2.22	1.99	2.10	1.91	1.86	1.90	1.51	1.69	2.60	2.57	1.84	1.80	1.59	1.55	1.44	1.37	1.63	1.69	1.67
Al_2O_3	9.07	9.11	8.11	8.54	8.10	8.57	9.50	8.37	9.00	8.86	9.18	8.82	8.11	8.49	8.96	9.02	8.77	8.74	8.32	9.02	9.08	8.68
FeO_{tot}	12.68	12.80	12.84	12.05	12.16	12.07	12.18	12.11	12.31	12.05	11.58	11.37	11.39	12.20	11.97	12.11	12.57	12.76	12.06	11.58	12.36	12.23
MnO	0.24	0.20	0.15	0.34	0.22	0.26	0.24	0.20	0.13	0.66	0.69	0.49	0.47	0.73	0.71	0.46	0.46	0.48	0.48	0.64	0.64	0.67
MgO	13.21	13.60	13.04	13.26	13.56	14.46	13.16	13.32	13.23	13.41	13.37	13.33	13.37	13.60	13.13	14.53	14.68	13.89	15.90	13.96	14.15	13.20
CaO	11.32	11.15	11.08	11.19	12.13	11.07	11.00	10.96	11.29	11.76	11.74	11.84	11.15	11.33	11.48	11.42	11.37	11.45	11.35	12.34	11.95	11.22
Na_2O	2.04	1.87	2.01	2.33	2.17	2.22	2.64	2.51	2.03	2.82	3.05	2.50	2.85	2.17	2.07	1.21	1.29	1.20	1.10	1.79	1.93	2.97
K_2O	0.62	0.56	0.59	0.58	0.55	0.59	0.95	0.91	0.53	0.37	0.44	0.97	0.97	0.52	0.45	0.85	0.94	0.86	0.74	0.32	0.37	0.36
Total	97.18	96.98	96.66	96.65	96.80	96.60	96.08	96.02	96.10	97.14	97.11	96.92	96.89	96.06	96.08	96.89	96.94	96.45	96.93	97.12	98.07	96.08
Si	6.477	6.47	6.633	6.567	6.623	6.54	6.392	6.582	6.493	6.512	6.459	6.499	6.624	6.55	6.493	6.49	6.514	6.527	6.584	6.494	6.487	6.521
Al^{IV}	1.523	1.53	1.367	1.433	1.377	1.46	1.608	1.418	1.507	1.488	1.541	1.501	1.376	1.45	1.507	1.51	1.486	1.473	1.416	1.506	1.513	1.479
Sum *T*-site	8	8	8	8	8	8	8	8	8	8	8	8	8	8	8	8	8	8	8	8	8	8
Al^{VI}	0	0	0	0	0	0	0	0	0	0	0	0	0	0	0	0	0	0	0	0	0	0
Ti	0.27	0.24	0.26	0.24	0.22	0.23	0.21	0.20	0.20	0.16	0.18	0.28	0.28	0.20	0.19	0.17	0.17	0.16	0.15	0.17	0.18	0.18
Fe^{3+}	0	0	0	0	0	0	0	0	0	0	0	0	0	0	0	0	0	0	0	0	0	0
Mg	2.81	2.89	2.78	2.81	2.92	3.12	2.82	2.86	2.80	2.85	2.84	2.87	2.87	2.94	2.79	3.08	3.15	2.96	3.42	2.95	2.98	2.85
Fe^{2+}	1.51	1.53	1.54	1.43	1.47	1.46	1.46	1.46	1.46	1.44	1.38	1.37	1.37	1.48	1.43	1.44	1.51	1.53	1.43	1.37	1.46	1.48
Mn^{2+}	0.03	0.02	0.02	0.04	0.03	0.03	0.03	0.02	0.02	0.08	0.08	0.06	0.06	0.09	0.09	0.06	0.06	0.06	0	0.08	0.08	0.08
Sum *C*-site	4.62	4.68	4.60	4.53	4.63	4.84	4.52	4.54	4.49	4.53	4.48	4.59	4.58	4.71	4.50	4.74	4.88	4.70	5.00	4.57	4.70	4.59
Mn^{2+}	0	0	0	0	0	0	0	0	0	0	0	0	0	0	0	0	0	0	0.059	0	0	0
Fe^{2+}	0	0	0	0	0	0	0	0	0	0	0	0	0	0	0	0	0	0	0.027	0	0	0
Ca	1.73	1.70	1.70	1.71	1.87	1.71	1.69	1.69	1.72	1.80	1.79	1.83	1.72	1.76	1.76	1.74	1.75	1.76	1.76	1.87	1.81	1.74
Na	0.27	0.30	0.30	0.29	0.13	0.29	0.31	0.31	0.28	0.20	0.21	0.17	0.28	0.24	0.25	0.26	0.25	0.25	0.16	0.13	0.19	0.26
Sum *B*-site	2	2	2	2	2	2	2	2	2	2	2	2	2	2	2	2	2	2	2	2	2	2
Na	0.29	0.22	0.26	0.35	0.48	0.34	0.43	0.39	0.28	0.58	0.63	0.53	0.52	0.37	0.33	0.07	0.11	0.09	0.15	0.37	0.34	0.57
Ca	0	0	0	0	0	0	0	0	0	0	0	0	0	0	0	0	0	0	0	0	0	0
K	0.11	0.10	0.11	0.11	0.10	0.11	0.17	0.17	0.10	0.07	0.08	0.18	0.18	0.10	0.08	0.15	0.17	0.16	0.14	0.06	0.07	0.07
Sum *A*-site	0.40	0.32	0.36	0.45	0.58	0.45	0.60	0.56	0.37	0.64	0.71	0.71	0.69	0.47	0.41	0.23	0.28	0.24	0.29	0.42	0.41	0.64

Table 6. (Continued).

Sample No.	DG-45	DG-45	DG-45	DG-45	DG-45	DG-45	DG-45	DG-45	DG-45	DG-4	DG-4	DG-4	DG-4	DG-4	DG-4	DG-4	DG-4	DG-4	DG-6	DG-6	DG-6	DG-6
OH	1.90	1.90	1.91	1.90	1.93	1.93	1.92	1.92	1.90	1.90	1.90	1.93	1.92	1.94	1.91	1.90	1.92	1.91	1.93	1.89	1.89	1.93
Sum cations	15.02	15.00	14.96	14.98	15.21	15.28	15.12	15.09	14.86	15.17	15.20	15.30	15.27	15.17	14.91	14.97	15.16	14.95	15.29	14.99	15.10	15.23
Cation charge	45.73	45.46	45.83	45.93	46.09	45.40	45.83	45.94	45.77	46.00	46.13	46.25	46.25	45.61	45.81	45.18	45.06	45.28	44.71	45.79	45.52	45.89
Mineral name	Ts	Ts	Mg-Hbl	Mg-Hbl	Mg-Hbl	Mg-Hbl	Ts	Mg-Hbl	Ts	Mg-Hbl	Ts	Ts	Mg-Hbl	Mg-Hbl	Ts	Ts	Mg-Hbl	Mg-Hbl	Mg-Hbl	Ts	Ts	Mg-Hbl
P (MPa) ± 17	183	183	146	163	148	161	212	159	183	177	193	179	148	162	183	176	166	168	145	180	178	173
T (°C) ± 14	867	865	834	851	862	868	885	850	857	874	891	896	866	863	863	862	864	852	875	876	874	870
H_2O melt (%) ± 0.7	5.25	5.36	5.01	5.08	4.88	4.18	4.28	3.92	5.79	5.39	5.32	4.06	3.44	5.00	6.05	5.05	4.30	5.18	4.43	6.32	5.79	5.06
ΔNNO ± 0.4	0.60	0.88	0.60	0.60	0.70	1.17	0.62	0.72	0.75	0.64	0.51	0.39	0.43	0.91	0.70	1.47	1.57	1.32	2.19	0.94	1.06	0.62
$\log fO_2 \pm 0.5$	-11.89	-11.64	-12.53	-12.20	-11.89	-11.31	-11.52	-12.10	-11.93	-11.73	-11.53	-11.56	-12.09	-11.66	-11.87	-11.12	-10.98	-11.47	-10.16	-11.39	-11.31	-11.82
Continental depth (km)	6.92	6.91	5.51	6.15	5.57	6.08	8.01	6.01	6.91	6.68	7.28	6.74	5.61	6.13	6.90	6.64	6.27	6.35	5.49	6.81	6.72	6.53

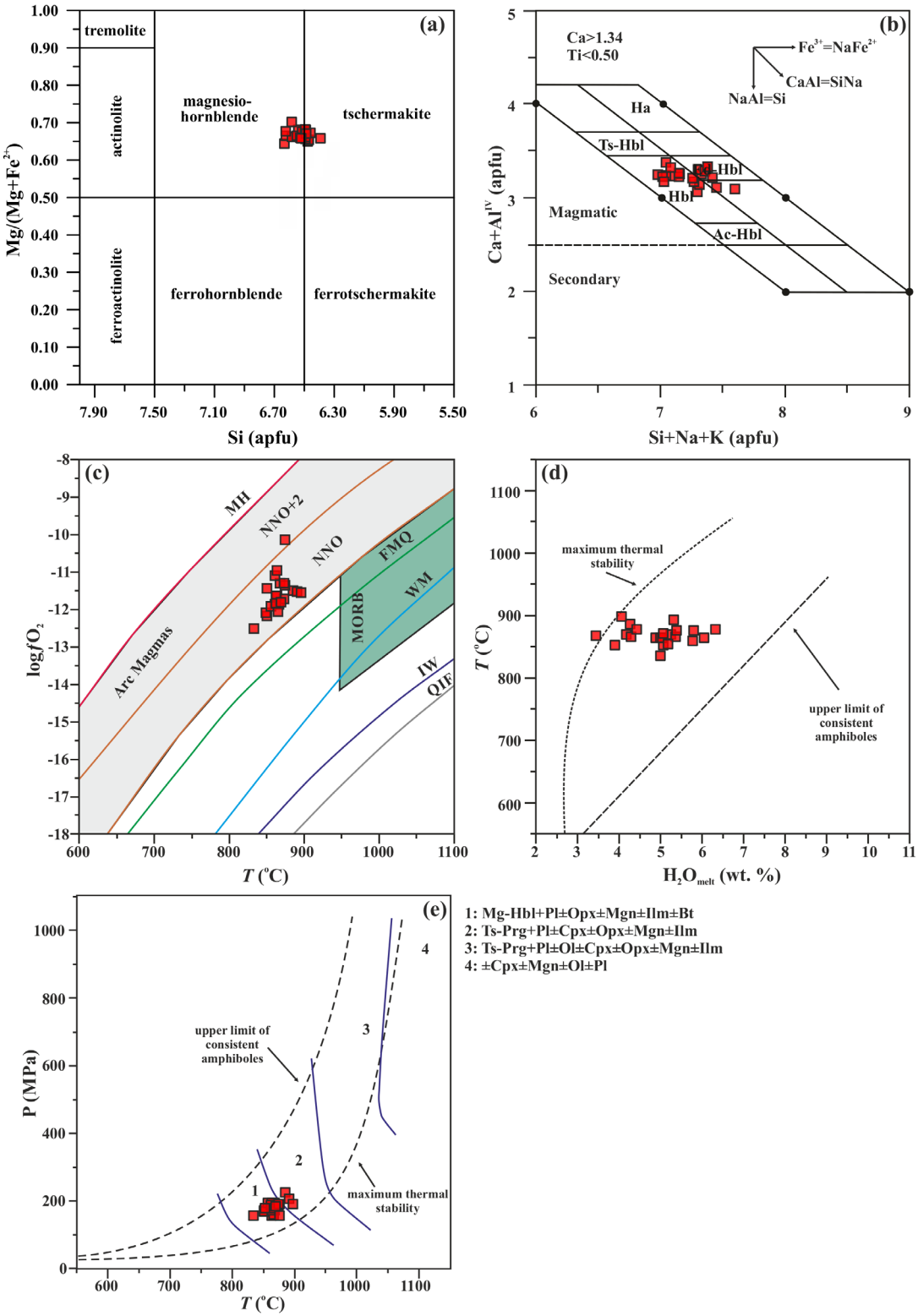

Figure 11. a) Si vs. Mg/(Mg+Fe^{2+}) and b) Si+Na+K vs. Ca+Al^{IV} (apfu) classification diagrams (Leak et al., 1997; Giret et al., 1980) of amphiboles from the Karadağ Pluton c) logfO_2–T diagram (Ridolfi et al., 2010 and modified by Aysal, 2015), d) T–H_2O melt diagram, and e) P–T diagram (Ridolfi et al., 2010) for the physicochemical condition of amphibole crystallization. Mg-hbl: magnesio hornblende; Opx: orthopyroxene; Mgn: magnetite; Ilm: ilmenite; Ts-Prg: tschermakite-pargasite; Cpx: clinopyroxene; Ol: olivine.

Table 7. Representative EPMA analyses results and calculated end-members of amphibole minerals.

Sample No.	**DG-45**	**DG-45**	**DG-45**	**DG-45**	**DG-45**	**DG-45**	**DG-45**	**DG-45**	**DG-45**	**DG-4**	**DG-4**	**DG-4**	**DG-4**	**DG-4**	**DG-4**	**DG-4**	**DG-4**	**DG-4**	**DG-6**	**DG-6**	**DG-6**	**DG-6**
Point No.	**1**	**2**	**3**	**4**	**5**	**6**	**7**	**8**	**9**	**1**	**2**	**3**	**4**	**5**	**6**	**7**	**8**	**9**	**1**	**2**	**3**	**4**
SiO_2	45.47	45.40	46.39	46.14	45.92	45.25	44.50	45.77	45.69	45.69	45.36	45.00	46.02	45.19	45.51	45.70	45.31	45.63	45.60	45.83	45.90	45.09
TiO_2	2.53	2.28	2.45	2.22	1.99	2.10	1.91	1.86	1.90	1.51	1.69	2.60	2.57	1.84	1.80	1.59	1.55	1.44	1.37	1.63	1.69	1.67
Al_2O_3	9.07	9.11	8.11	8.54	8.10	8.57	9.50	8.37	9.00	8.86	9.18	8.82	8.11	8.49	8.96	9.02	8.77	8.74	8.32	9.02	9.08	8.68
FeO_{tot}	12.68	12.80	12.84	12.05	12.16	12.07	12.18	12.11	12.31	12.05	11.58	11.37	11.39	12.20	11.97	12.11	12.57	12.76	12.06	11.58	12.36	12.23
MnO	0.24	0.20	0.15	0.34	0.22	0.26	0.24	0.20	0.13	0.66	0.69	0.49	0.47	0.73	0.71	0.46	0.46	0.48	0.48	0.64	0.64	0.67
MgO	13.21	13.60	13.04	13.26	13.56	14.46	13.16	13.32	13.23	13.41	13.37	13.33	13.37	13.60	13.13	14.53	14.68	13.89	15.90	13.96	14.15	13.20
CaO	11.32	11.15	11.08	11.19	12.13	11.07	11.00	10.96	11.29	11.76	11.74	11.84	11.15	11.33	11.48	11.42	11.37	11.45	11.35	12.34	11.95	11.22
Na_2O	2.04	1.87	2.01	2.33	2.17	2.22	2.64	2.51	2.03	2.82	3.05	2.50	2.85	2.17	2.07	1.21	1.29	1.20	1.10	1.79	1.93	2.97
K_2O	0.62	0.56	0.59	0.58	0.55	0.59	0.95	0.91	0.53	0.37	0.44	0.97	0.97	0.52	0.45	0.85	0.94	0.86	0.74	0.32	0.37	0.36
Total	97.18	96.98	96.66	96.65	96.80	96.60	96.08	96.02	96.10	97.14	97.11	96.92	96.89	96.06	96.08	96.89	96.94	96.45	96.93	97.12	98.07	96.08
Si	6.477	6.47	6.633	6.567	6.623	6.54	6.392	6.582	6.493	6.512	6.459	6.499	6.624	6.55	6.493	6.49	6.514	6.527	6.584	6.494	6.487	6.521
Al^{IV}	1.523	1.53	1.367	1.433	1.377	1.46	1.608	1.418	1.507	1.488	1.541	1.501	1.376	1.45	1.507	1.51	1.486	1.473	1.416	1.506	1.513	1.479
Sum *T*-site	8	8	8	8	8	8	8	8	8	8	8	8	8	8	8	8	8	8	8	8	8	8
Al^{VI}	0	0	0	0	0	0	0	0	0	0	0	0	0	0	0	0	0	0	0	0	0	0
Ti	0.27	0.24	0.26	0.24	0.22	0.23	0.21	0.20	0.20	0.16	0.18	0.28	0.28	0.20	0.19	0.17	0.17	0.16	0.15	0.17	0.18	0.18
Fe^{3+}	0	0	0	0	0	0	0	0	0	0	0	0	0	0	0	0	0	0	0	0	0	0
Mg	2.81	2.89	2.78	2.81	2.92	3.12	2.82	2.86	2.80	2.85	2.84	2.87	2.87	2.94	2.79	3.08	3.15	2.96	3.42	2.95	2.98	2.85
Fe^{2+}	1.51	1.53	1.54	1.43	1.47	1.46	1.46	1.46	1.46	1.44	1.38	1.37	1.37	1.48	1.43	1.44	1.51	1.53	1.43	1.37	1.46	1.48
Mn^{2+}	0.03	0.02	0.02	0.04	0.03	0.03	0.03	0.02	0.02	0.08	0.08	0.06	0.06	0.09	0.09	0.06	0.06	0.06	0	0.08	0.08	0.08
Sum *C*-site	4.62	4.68	4.60	4.53	4.63	4.84	4.52	4.54	4.49	4.53	4.48	4.59	4.58	4.71	4.50	4.74	4.88	4.70	5.00	4.57	4.70	4.59
Mn^{2+}	0	0	0	0	0	0	0	0	0	0	0	0	0	0	0	0	0	0	0.059	0	0	0
Fe^{2+}	0	0	0	0	0	0	0	0	0	0	0	0	0	0	0	0	0	0	0.027	0	0	0
Ca	1.73	1.70	1.70	1.71	1.87	1.71	1.69	1.69	1.72	1.80	1.79	1.83	1.72	1.76	1.76	1.74	1.75	1.76	1.76	1.87	1.81	1.74
Na	0.27	0.30	0.30	0.29	0.13	0.29	0.31	0.31	0.28	0.20	0.21	0.17	0.28	0.24	0.25	0.26	0.25	0.25	0.16	0.13	0.19	0.26
Sum *B*-site	2	2	2	2	2	2	2	2	2	2	2	2	2	2	2	2	2	2	2	2	2	2
Na	0.29	0.22	0.26	0.35	0.48	0.34	0.43	0.39	0.28	0.58	0.63	0.53	0.52	0.37	0.33	0.07	0.11	0.09	0.15	0.37	0.34	0.57
Ca	0	0	0	0	0	0	0	0	0	0	0	0	0	0	0	0	0	0	0	0	0	0
K	0.11	0.10	0.11	0.11	0.10	0.11	0.17	0.17	0.10	0.07	0.08	0.18	0.18	0.10	0.08	0.15	0.17	0.16	0.14	0.06	0.07	0.07
Sum *A*-site	0.40	0.32	0.36	0.45	0.58	0.45	0.60	0.56	0.37	0.64	0.71	0.71	0.69	0.47	0.41	0.23	0.28	0.24	0.29	0.42	0.41	0.64

Table 7. (Continued).

OH	1.90	1.90	1.91	1.90	1.93	1.93	1.92	1.92	1.90	1.90	1.90	1.93	1.92	1.94	1.91	1.90	1.92	1.91	1.93	1.89	1.89	1.93
Sum Cations	15.02	15.00	14.96	14.98	15.21	15.28	15.12	15.09	14.86	15.17	15.20	15.30	15.27	15.17	14.91	14.97	15.16	14.95	15.29	14.99	15.10	15.23
Cation Charge	45.73	45.46	45.83	45.93	46.09	45.40	45.83	45.94	45.77	46.00	46.13	46.25	46.25	45.61	45.81	45.18	45.06	45.28	44.71	45.79	45.52	45.89
Mineral name	Ts	Ts	Mg-Hbl	Mg-Hbl	Mg-Hbl	Mg-Hbl	Ts	Mg-Hbl	Ts	Mg-Hbl	Ts	Ts	Mg-Hbl	Mg-Hbl	Ts	Ts	Mg-Hbl	Mg-Hbl	Mg-Hbl	Ts	Ts	Mg-Hbl
P (MPa) ± 17	183	183	146	163	148	161	212	159	183	177	193	179	148	162	183	176	166	168	145	180	178	173
T (°C) ± 14	867	865	834	851	862	868	885	850	857	874	891	896	866	863	863	862	864	852	875	876	874	870
H_2Omelt (%) ± 0.7	5.25	5.36	5.01	5.08	4.88	4.18	4.28	3.92	5.79	5.39	5.32	4.06	3.44	5.00	6.05	5.05	4.30	5.18	4.43	6.32	5.79	5.06
ΔNNO ± 0.4	0.60	0.88	0.60	0.60	0.70	1.17	0.62	0.72	0.75	0.64	0.51	0.39	0.43	0.91	0.70	1.47	1.57	1.32	2.19	0.94	1.06	0.62
logfO_2 ± 0.5	-11.89	-11.64	-12.53	-12.20	-11.89	-11.31	-11.52	-12.10	-11.93	-11.73	-11.53	-11.56	-12.09	-11.66	-11.87	-11.12	-10.98	-11.47	-10.16	-11.39	-11.31	-11.82
Continental Depth (km)	6.92	6.91	5.51	6.15	5.57	6.08	8.01	6.01	6.91	6.68	7.28	6.74	5.61	6.13	6.90	6.64	6.27	6.35	5.49	6.81	6.72	6.53

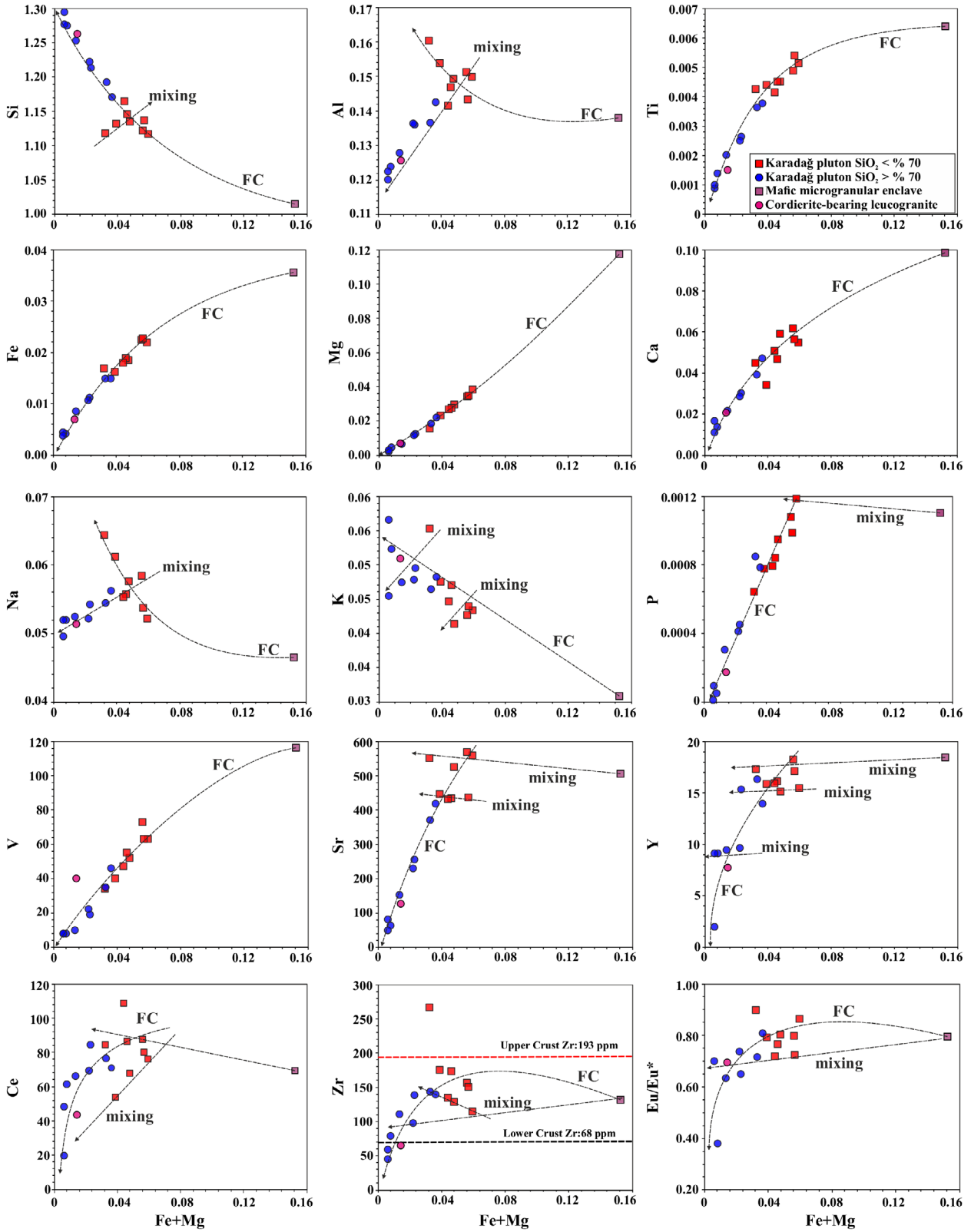

Figure 12. Mafic index (Fe+Mg) vs. major and trace element variation diagrams for the Karadağ Pluton (Zr values of upper and lower crust are from Rudnick and Gao, 2003).

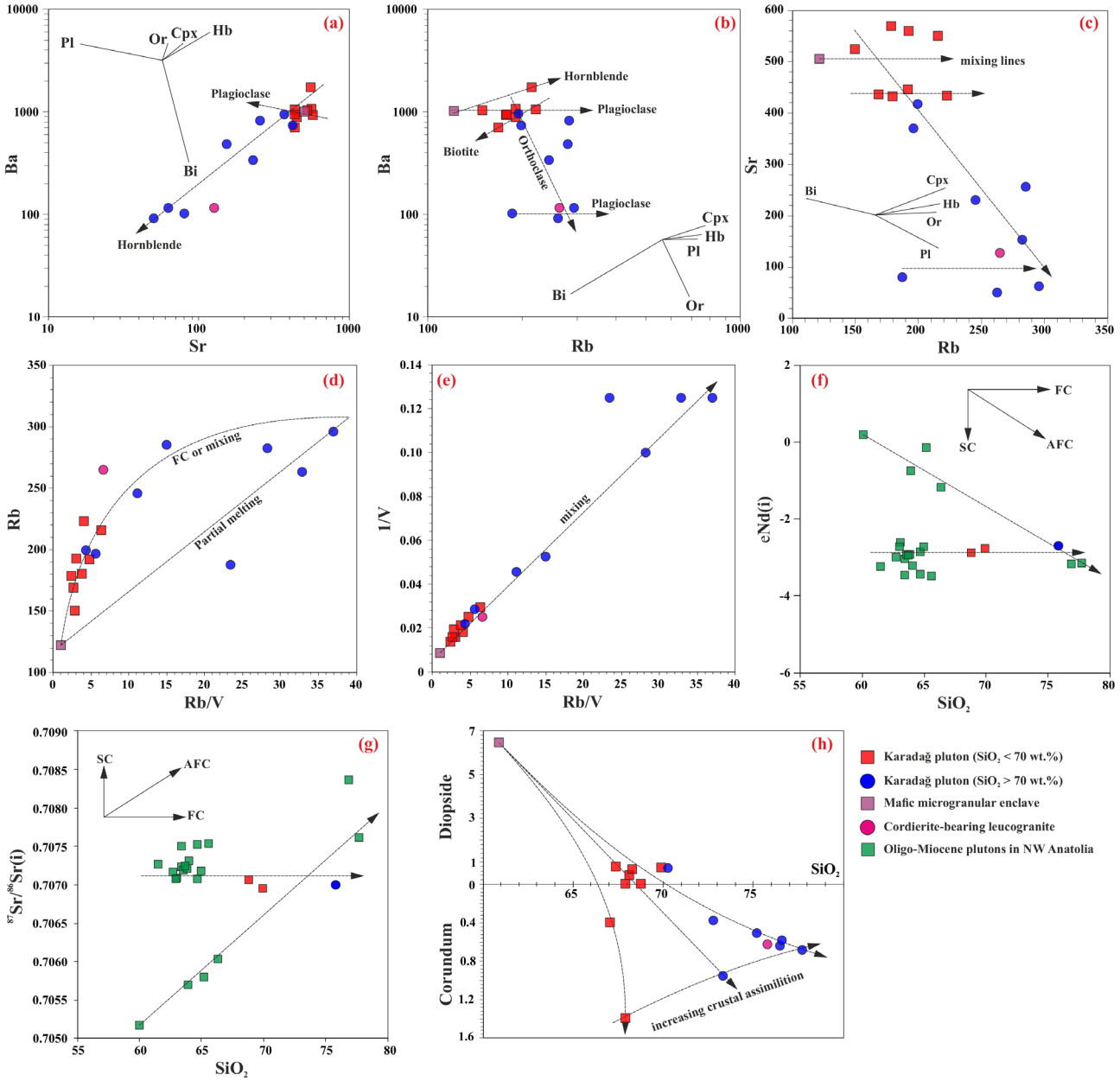

Figure 13. Modelling of magma evolution processes: a) Sr vs. Ba, b) Rb vs. Ba, and c) Rb vs. Sr diagrams for the FC of the Karadağ Pluton. d) Rb/V vs. Rb and e) Rb/V vs. 1/V diagrams, f) SiO_2 vs. eNd and SiO_2 vs. $^{87}Sr/^{86}Sr_i$ and SiO_2 vs. normative corundum+diopside for the partial melting, FC and mixing processes of the Karadağ Pluton.

tures are found on both the host plutonic bodies and the enclaves, and they represent a composition resorption or dissolution process (Figures 14a and 14b). Hibbard (1995) argued that boxy-cellular plagioclase crystals were formed as a result of mixing of hot-mafic magma-derived plagioclase with cold felsic magma. This study also implied that as the process continued, only the patches of the original Ca-rich plagioclase remained largely isolated in the non-cellular Na-rich plagioclase crystal. On the other hand, the mixing of reinjected mafic magma and felsic magma-derived plagioclase caused cellular melting in the plagioclase, and formed spongy-cellular plagioclase crystals (Hibbard, 1995). The mantled feldspars were represented by 2 main textures, defined as rapakivi and antirapakivi textures. Rapakivi texture was represented by K-feldspar mantled by the plagioclase, which had a concentric zone. While

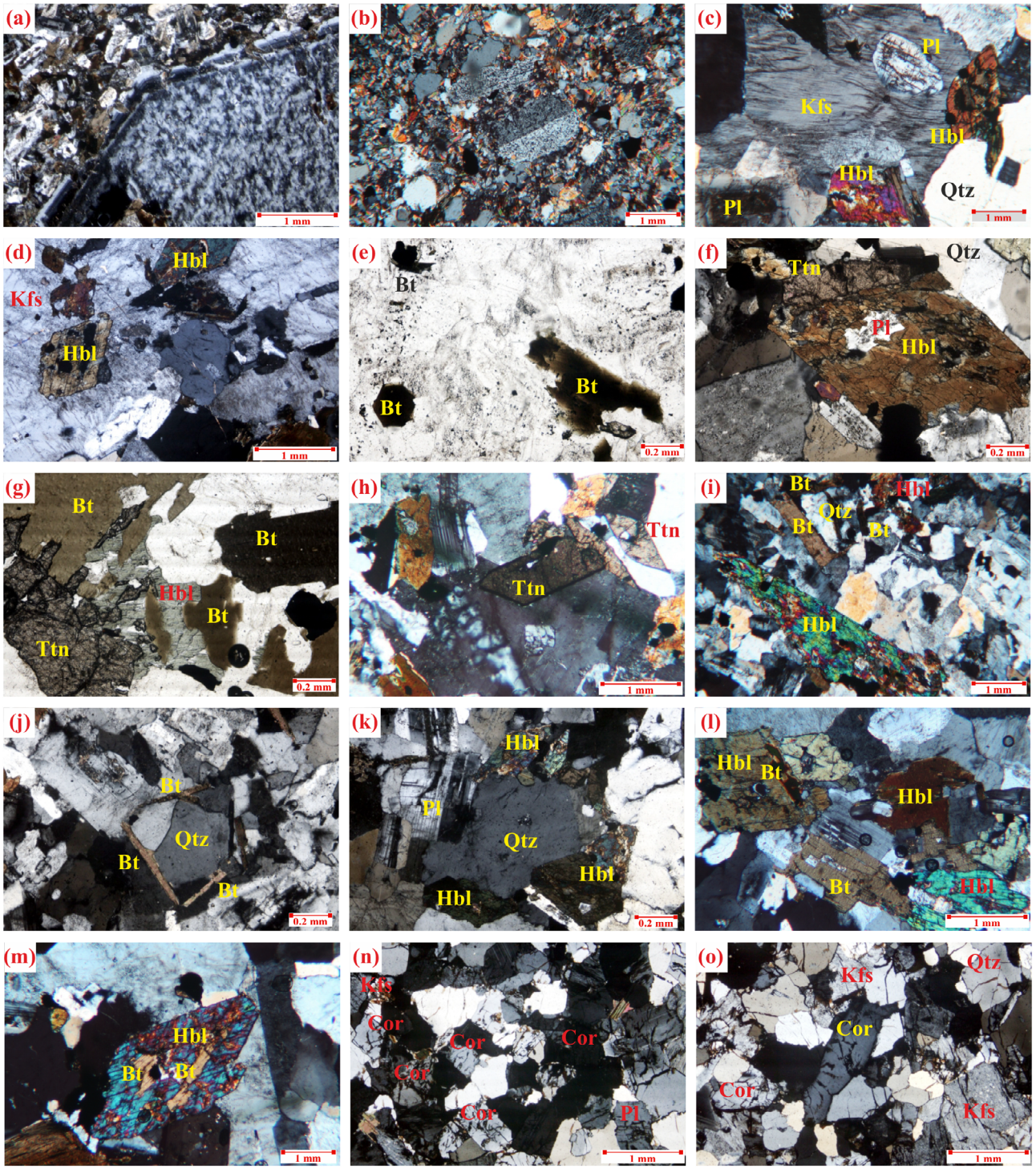

Figure 14. Thin-section photographs of various magma mixing textures and peritectic phase entrainment from the Karadağ Pluton: a-b) sponge cellular plagioclase in the MMEs and their host rocks, c) anti-rapakivi texture, d) poicilitic textured K-feldspar and mafic mineral inclusions, e) blade-shaped and pseudohexagonal biotite, f) appinitic texture (plagioclase into hornblende), g) biotite destabilization texture, h) titanite-centered ocellar texture, i-j) biotite-quartz ocellar texture, k) hornblende-quartz ocellar texture, l-m) biotite-hornblende disequilibrium texture, and n-o) K-feldspar-cordierite peritectic mineral assemblages. Ttn: titanite; Cor: cordierite.

the K-feldspar crystals were up to 3–6 cm in length, plagioclase rims were narrow areas with a width of 1–3 mm (Figures 3g and 3h). During the mixing of the 2 different (mafic and felsic) magma batches, K-feldspar crystals in the felsic magma formed a crystallization nucleus base for the plagioclase (Hibbard, 1991). Antirapakivi texture was represented by plagioclase cores and K-feldspar mantles (Figure 14c). The formation of antirapakivi-textured feldspars can be explained in different ways, such as 1) mafic magma-derived solid plagioclase crystals mantled by K-feldspar in felsic magma, and 2) when the peritectic-like region of the liquidus surface was reached, the nearby plagioclases reacted with the melt to produce K-feldspar and thus, was mantled by the growing K-feldspar (Nakano, 1992). Coarse-grained K-feldspar and plagioclase crystals showed a poikilitic texture and enclosed small mafic and felsic minerals that had previously formed, such as hornblende, biotite, and plagioclase, as inclusions (Figure 14d). Blade-shaped biotites (Figure 14e) are often a result of the magma mixing, and they are the early crystalline phases in which the growth of biotite in a mafic system is physically limited by the felsic system (Hibbard, 1991). Acicular apatite minerals are often found together with mafic mineral assemblages, such as hornblende, and represent rapid growth as the result of magma mixing and rapid cooling of mafic magma (Hibbard, 1991). In addition, the Karadağ Pluton samples included other special textures as well, such as an appinitic texture (Ayrton, 1991), euhedral hornblende minerals with plagioclase in the center (Figure 14f), biotite destabilization textures (Figure 14g) with embayment occupied by plagioclase, and small titanite crystals related to magma mixing processes (Vegas et al., 2011). The titanite-centered ocellar texture (Figure 14h), which is one of the typical textures of hybrid intermediate rocks, consists of leucocratic ocelli with titanite crystals at the center, is enclosed in a mafic mineral-rich matrix, and it indicates that this texture was represented hybrid intermediate rocks (Vegas et al., 2011). Quartz-biotite ocellar textures (Figures 14i and 14j) and hornblende-quartz ocellar textures (Figure 14k) are defined as a result of interactions between different magmas with mafic and felsic composition (Hibbard, 1991). Dissolving quartz minerals along their edges decreases the crystallization temperature of melts, which causes local rapid cooling and nucleation of mafic minerals (Baxter and Feely, 2002). The new thermal and physical conditions with compositional variability that arise as a result of mixing of mafic and felsic magmas can be recognized by various mineral disequilibrium textures, such as hornblende and biotite disequilibrium (Figures 14l and 14m).

Major and trace element behaviors play a key role in monitoring magma mixing processes. The linear trends on bivariate major and trace element Harker variation diagrams reflect different magma mixtures and magma replenishment processes in open magmatic systems. In the major and trace element vs. mafic index of Harker variation diagrams, some elements, such as Si, Al, Na, K, P, Sr, Y, Ce, Zr, and Eu, showed a typical mixing trend, represented by cross-orientations in the element evolutionary trend. For Rb-Sr, the Rb/V vs. Rb, and Rb/V vs. 1/V diagrams (Figures 13d and 13e) showed that the Karadağ Pluton was affected by the magma mixing processes between mafic and felsic magmas. Using biotite mineral chemistry data, especially the ΣFeO/(ΣFeO+MgO) and MgO contents can be used to describe different origins of the biotite (Zhou, 1986). Mineral chemistry analyses of the biotites of the Karadağ Pluton clearly showed the mixture of crusts and mantle-derived melts (Figure 10e).

5.2.3. Peritectic assemblage entrainment

Peritectic assemblage entrainment in granitic magmas is represented by a series of mineral assemblages, such as orthopyroxene, clinopyroxene, K-feldspar, garnet, and cordierite. The breakdown of hydrous minerals, such as hornblende, biotite, and muscovite, provides fluid to melts and causes incongruent mineral reactions that produce anhydrous peritectic minerals, such as orthopyroxene, clinopyroxene, K-feldspar, garnet, cordierite, sillimanite, and/or kyanite (Yakymchuk, 2019 and references therein). The breakdown-melting of hydrous minerals and new peritectic mineral production depends on pressure and temperature. However, muscovite-breakdown melting produces K-feldspar, sillimanite, and/or kyanite in the peritectic mineral phase at low temperatures, the biotite-breakdown melting begins after depletion of the muscovite, and the peritectic mineral assemblages are represented by orthopyroxene, K-feldspar, garnet, and cordierite. In addition, hornblende-breakdown melting produces clinopyroxene, orthopyrexene and garnet as peritectic phase at relatively high temperatures and under variable pressure conditions in fluid-absent systems (Thompson, 1982; Clemens, 2006; Moyen and Stevens, 2006; Palin et al., 2016; Yakymchuk, 2019). In the absence of peritectic mineral assemblages in fluid-present systems, the fluid-present reactions are congruent and some minerals, such as quartz and feldspar, are used as a reactant in this system. However, the hydrous (hornblende) and anhydrous (garnet) peritectic minerals can also be produced within this system (Yakymchuk, 2019 and references therein).

Peritectic assemblage entrainment was represented by the coexistence of K-feldspar and cordierite in the Karadağ Pluton samples (Figures 14n, 14o, and 15). Different generation models have been proposed for the origin of the cordierite in felsic-peraluminous igneous rocks as reported by Clarke (1995). One model suggested that the cordierite may have had a metamorphic origin and been incorporated in the system in 2 different ways, such as xe-

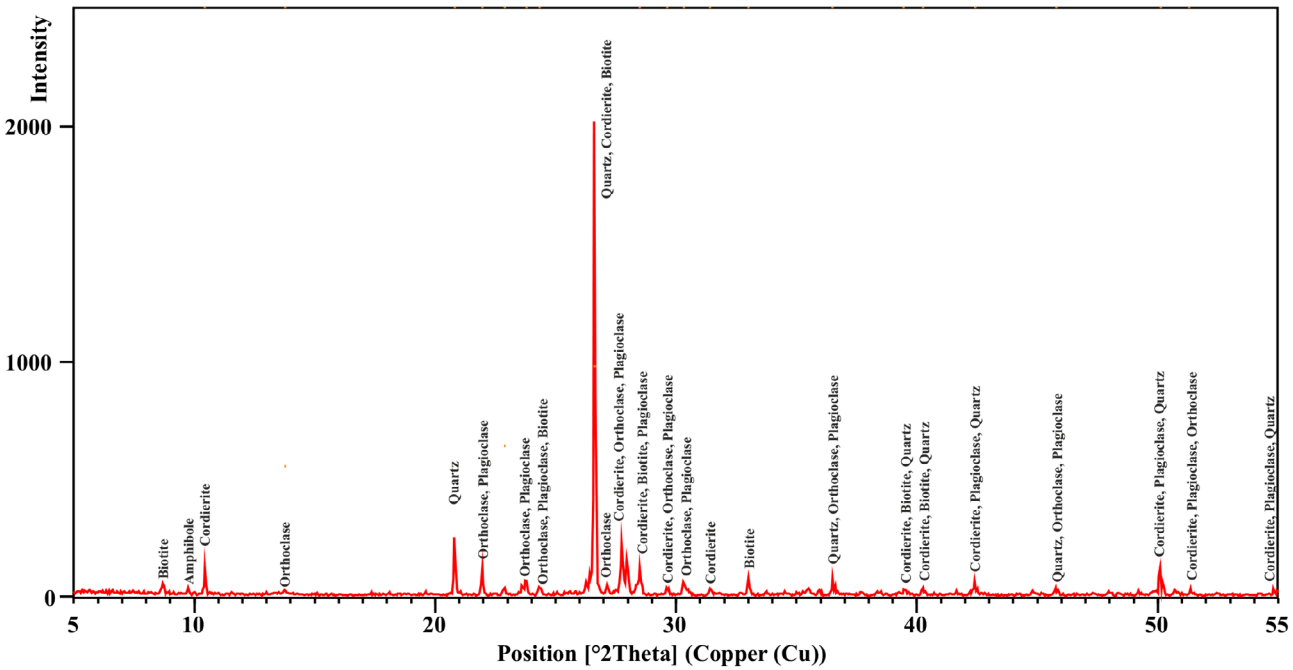

Figure 15. Representative XRD patterns of the cordierite-bearing leucogranite sample from the Karadağ Pluton.

nocrystic and restitic incorporation. Another model proposed that the cordierite had a magmatic origin and could occur in different forms, such as peritectic, cotectic, and pegmatitic. The last model implied a metasomatic generation (Clarke, 1995). Granitic magmas generally intrude into metamorphic rocks in the lower and upper crust and they can include wall-rock fragments, such as xenoliths. If the wall-rock has a pelitic origin, it might already contain cordierite and other aluminosilicate minerals, such as andalusite and/or sillimanite. On the other hand, andalusite and cordierite are common contact metamorphic minerals in pelitic country-rocks. However, some petrographic features still allow the recognition of xenolithic cordierite formations associated with wall-rock assimilation, such as the chemical composition of cordierite, its crystal shape, and inclusion types (Clarke, 1995).

Recent studies have shown that peritectic phase entrainment plays an important role in the genesis and evolution of granitic magmas, as well as FC, assimilation, and magma mixing-mingling processes (Clemens and Stevens, 2012; Clemens and Philips, 2020). Moreover, some researchers have conducted new studies that have discussed the role of FC, assimilation, and magma mixing in granitic magma generation (Clemens et al., 2009; Clemens and Stevens, 2012; Clemens and Philips, 2020). They argued that there was a serious suspicion as to whether major variations in granitic magma formation were produced, in particular, by any differentiation mechanism. They also implied that peritectic phase entrainment in the source may be responsible for the generation of compositionally distinct magmas (Stevens et al., 2007; Taylor and Stevens, 2010; Clemens and Stevens, 2012). Consequently, FC, AFC, and magma mixing-mingling are the main magma chamber processes that occur within the upper crustal level (these are not processes occurring at the source) during magma ascent and emplacement in the cooling stage of the magma. Moreover, they carry the peritectic phase entrainment traces of the source (Clemens and Philips, 2020 and references therein). Recent experimental petrology studies (i.e. Erdman et al., 2010) have shown that wall-rock assimilations can play an important role in the formation of peritectic mineral assemblages. Erdman et al. (2010) suggested that if magmas were contaminated by the wall-rocks, a melt could be formed that included peritectic minerals that had been formed by incongruent melting or dissolution of original contaminants. They also implied that providing xenoliths and xenocrystals additives could be observed within that magma (xenocrysts ± host melt = peritectic crystal(s) + melt). Moreover, they argued that it was difficult to identify the peritectic minerals and the former melt compositions in igneous rocks during these processes, and even emphasized that the peritectic mineral

phase could disappear if the magma residence times were extended in open magmatic systems.

The igneous peritectic assemblage only contained cordierite, which occurred as a result of the reaction that was produced in the melt in response to increasing temperatures. The reaction was defined as Als+Bt+Qz→L+Kfs+Crd (Clarke, 1995). In fact, this reaction was highly compatible with the mineral paragenesis of the cordierite-bearing peritectic phase observed in the Karadağ Pluton. During melting of pelitic and semi-pelitic rocks, cordierite and feldspar formations may be accompanied by the formation of plagioclase, garnet, and orthopyroxene. Clarke (1995) described the reactions for these phases as follows: Als+Bt+Pll+Qz→L+Crd+Kfs+P12, Als+Bt+Qz→L+Kfs+Crd+Grt, and Bt+Qz→L+Kfs+Crd+Opx (Als: aluminosilicate, Bt: biotite, Pl: plagioclase, Qz: quartz, Kfs: K-feldspar, Crd: cordierite, Grt: garnet, Opx: orthopyroxene, L: liquid).

The Karadağ Pluton intruded into the pelitic rocks of the Orhanlar Greywacke, and assimilated xenolith fragments. Therefore, other reactions involving cordierite and feldspar are likely to have occurred. The absence of garnet- and orthopyroxene-bearing peritectic assemblages in the Karadağ Pluton may have been due to incomplete reactions and/or an inability to reach suitable temperature and pressure conditions. The presence of cordierite with K-feldspar, as a peritectic mineral, can be interpreted as consistent with a fluid-present system. On the other hand, peritectic mineral assemblages with cordierite and K-feldspar coexistence are compatible with incongruent melting of the crust in a fluid-present system. Kamacı and Altunkayanak (2020) defined a garnet-bearing peritectic phase related to fluid-absent muscovite dehydration melting in 2 mica leucogranites of the Çataldağ Pluton, east of the Biga Peninsula, and consequently, they may have occurred under corresponding conditions.

5.2.4. Source of the magma

Experimental petrology studies on different rock types, such as greywackes, pelitic rocks, and mafic-intermediate igneous rocks, have provided important evidence for understanding the origins of igneous rocks (Patiño Douce, 1999; Altherr et al., 2000; Altherr and Siebel, 2002). In the K-Na-Ca ternary diagram (proposed by Farina et al., 2012), most samples from the Karadağ Pluton showed a similar pattern, with experimental melts of pelitic, greywacke and volcaniclastic greywacke (Figure 16a), and the Elba Island plutonic rocks. Moreover, this diagram indicated that the sources of the Karadağ Pluton were related to the interaction of melts derived from pelitic, greywacke, and volcaniclastic greywacke sources with mafic magmas. In the Al_2O_3-(Na_2O+K_2O)-CaO-FeO_t+MgO ternary diagram of Zhu et al. (2020), samples of the Karadağ Pluton were plotted within the I- and S-type magma fields, and gradually shifted from I-type to S-type fields (Figure 16b). When the samples were plotted in the Al_2O_3/(FeO_t+MgO)-3∗CaO-5∗(K_2O/Na_2O) ternary diagram of Laurent et al. (2014), major oxides of the Karadağ Pluton samples fell into the field of partial melting of high-K mafic rocks and tonalite (Figure 16c). In the F-An-Or diagram of Castro (2013), all of the samples fell into the low- and high-pressure water-undersaturated granites field (Figure 16d). In addition, all of the granite samples were characterized by the common presence of hornblende and plagioclase (± biotite) over a wide temperature range along the cotectic line (0.3 GPa – 2.5 wt.% H_2O). Moreover, peritectic reaction boundaries between pyroxene-hornblende (p1) and hornblende-biotite (p2) are shown on the diagram, and the Karadağ Pluton samples were close to p2. However, it can be seen that the more felsic leucogranite samples evolved towards the eutectic point, and were reflected in the textural properties of these rocks, as shown in the petrography section (Figure 4f). As a result, the Karadağ Pluton was formed by the gradual mixing of melts derived from a high K calc-alkaline mafic source (enriched mantle source and/or lower crust) with peraluminous melts derived from upper crustal sources in a shallow magma chamber.

The selective enrichment in LILEs and LREEs, with a distinct depletion in Ta and Nb, and depleted HFSEs on the N-MORB normalized multielement spider diagram indicated that their genesis was related to hydrous melting of a mantle wedge in a subduction zone. In addition, enrichment in LILEs and depletion in HFSEs could have been related to a postcollisional tectonic setting and/or arc-related geochemical signature (Pearce, 1983). However, similar multielement patterns can be observed in mantle-derived magmas contaminated by the crust-derived magmas in collision zones, developed during the latest stages of the subduction, or can be also enriched during previous subduction (Pearce et al, 1990). When the subducting oceanic crust reaches a certain depth, LILE-rich fluids are released due to dehydration in the subduction zones. The Karadağ Pluton samples had relatively high Th/Yb and Ba/La values (Figure 8c). While high Th/Yb ratios show a significant addition of sediment-derived melts, relatively high Ba/La ratios suggest that fluid metasomatism played an important role in melt generation. The depleted mantle wedge was metasomatized due to the entry of these fluids, and formed the melts of fluid-rich mafic magmas (Pearce, 1983). The underplating of fluid-rich mafic magmas under the lower crust provided the heat and fluid source necessary for the crustal melting (Annen et al., 2006). Castro (2013) argued that granitic magmas derived from deep sources were more felsic than reequilibrated magmas under low pressure conditions, and that water-unsaturated granite magmas may originate from the lower continental crust or deeper lithospheric mantle. In

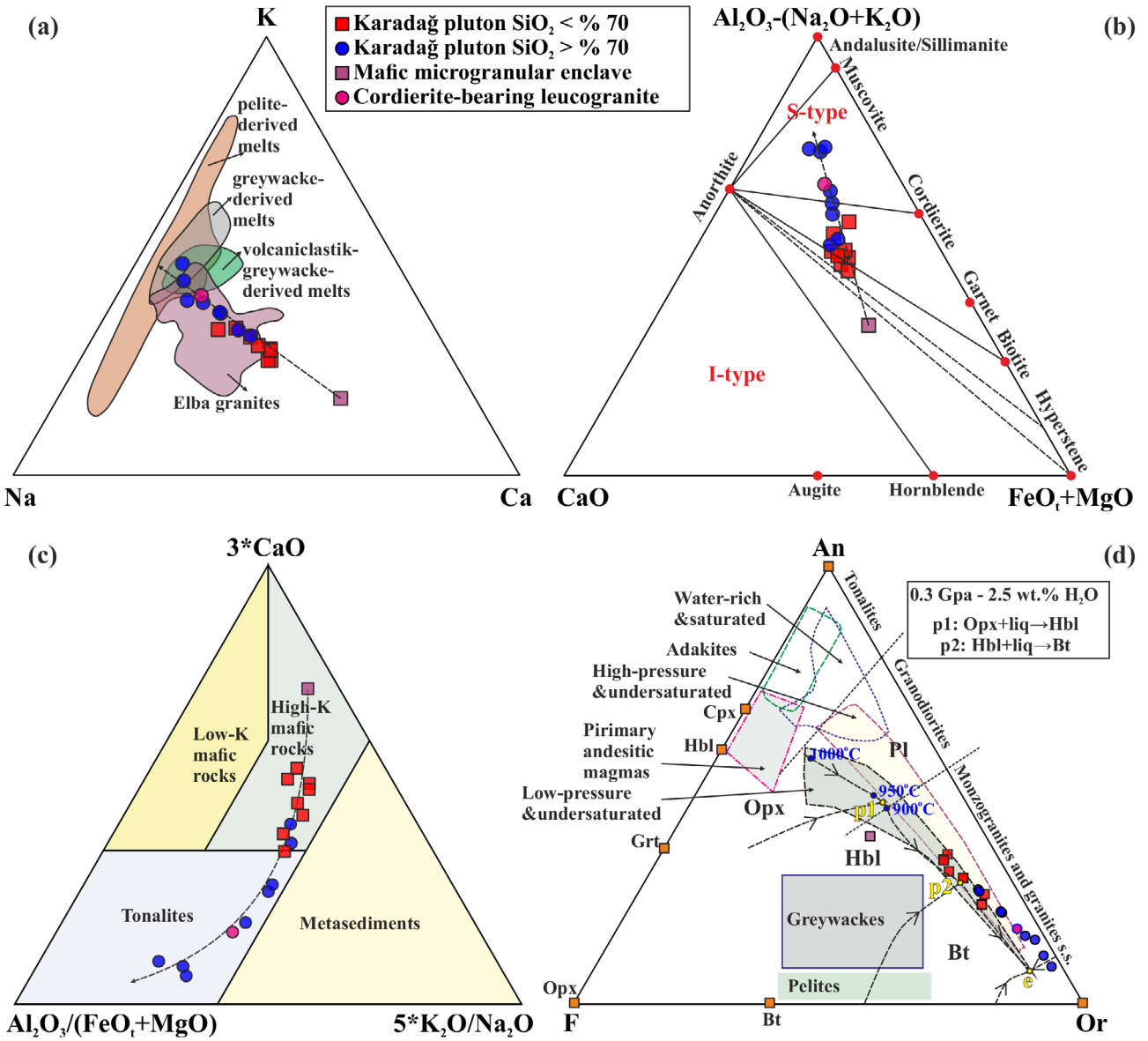

Figure 16. Ternary classification diagrams for the source of magma and compositionally evolution of the Karadağ Pluton: a) K-Na-Ca ternary diagram (experimental melts and the Elba Pluton data were from Farina et al., 2012), b) Al_2O_3-(Na_2O+K_2O))–CaO–FeO_T+MgO ternary diagram (Zhu et al., 2020), and c) Al_2O_3/(FeO_t+MgO)–3∗CaO–5∗(K_2O/Na_2O) ternary diagram of the Laurent et al. (2014), d) F–An–Or (F=FeO + MgO + MnO) ternary diagram of Castro (2013).

addition, Castro (2013) implied that mafic magmas were derived from metasomatized mantle, and that their high water content was effective on the texture of these rocks, such as euhedral hornblende. Black et al. (2013) argued that granitic magmas were formed by the dehydration of subducting slabs, which induced fluid-flux melting of the lithospheric mantle and partial melting of the overlying Sakarya Zone.

The initial $^{87}Sr/^{86}Sr$ and $^{143}Nd/^{144}Nd$ ratios and εNd(T) values suggested an enriched lithospheric mantle source (Figure 9). On the other hand, the Nd and Sr isotope data of the Karadağ Pluton samples showed an evolutionary trend similar to the other Oligo-Miocene plutonic rocks in the Biga Peninsula, and they indicated that the Karadağ Pluton was mainly affected by FC, assimilation, as clearly represented by the subduction zone enrichment (Figures 13f and 13g). In the chondrite-normalized REE diagrams, the negative Eu anomalies indicated the importance of plagioclase fractionation. On the other hand, the gradually increase of the negative Eu anomaly towards more felsic

samples showed that FC was the dominant processes in all of the samples. Therefore, the upward-concave pattern in the REE diagram showed that middle REEs (MREEs) were partitioned into amphiboles and implied the dominant process of amphibole fractionation. Hence, the Sr-Nd isotopic data suggested dominant lithospheric mantle-derived melts for the Karadağ Pluton, which were likely to have interacted with the crust-derived melts (Figure 13).

All of the data presented above suggested that the Karadağ Pluton formed by the mixture of mantle-derived mafic and crustal felsic magmas at different degrees during the intrusive stages of the magma evolution in an ACM and/or a postcollision setting, which was mainly governed by the northward subduction of the Hellenic slab beneath the Sakarya Zone (Figure 17).

6. Conclusion

The Karadağ Pluton displays complex lithological, petrographical, and geochemical properties, and intrudes into the basement rocks of the Sakarya Zone in the Central Biga Peninsula. Based on the petrographic and geochemical features, 2 main rock groups were defined, as main plutonic facies (SiO_2 <70 wt.%) and late-stage, more felsic facies (SiO_2 >70 wt.%).

The K/Ar and U/Pb LA-ICP-MS zircons yielded ages between 20.2 ± 0.9 and 23.9 ± 0.5 Ma (Late Oligocene-Early Miocene) for the Karadağ Pluton.

Based on the petrographic and geochemical data, the Karadağ Pluton reflected peritectic assemblage entrainment in the source, and magma evolution processes, such as FC, magma mixing-mingling, and AFC during magma ascent and emplacement.

The mineral chemistry data suggested that the Karadağ Pluton was emplaced and evolved in shallow magma chambers in the upper crust at a depth of about 6.5 km.

The Karadağ Pluton was formed by the mixing of mantle-derived mafic and crust-derived felsic magmas in an ACM and/or a postcollision setting, closely related to the northward subduction of the Hellenic slab beneath the Sakarya Zone.

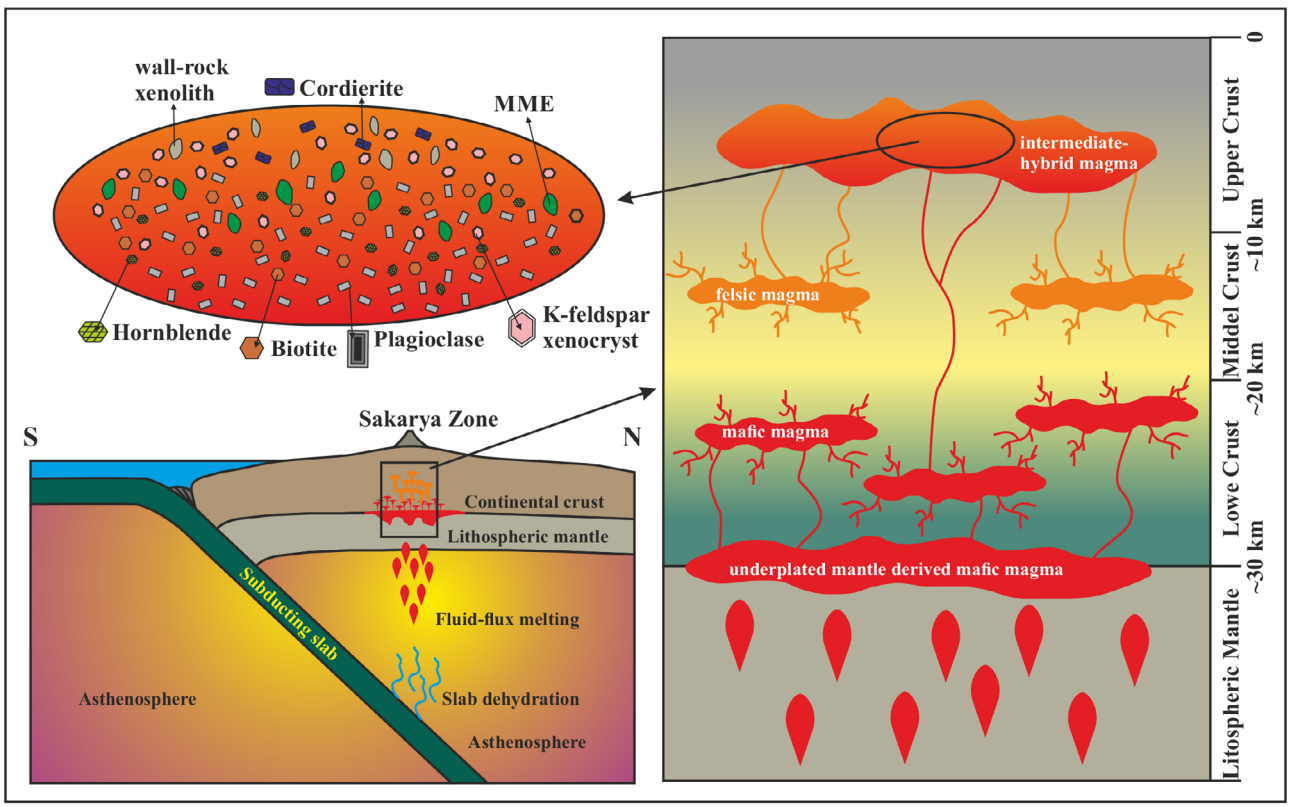

Figure 17. Possible geodynamic models showing magma generation and evolution processes of the Karadağ Pluton within the context of the Hellenic subduction system and magma chamber evolution (not scaled).

Acknowledgments
This work was supported by the Research Fund of İstanbul University-Cerrahpaşa, project numbers 25899 and 436/13092005. We thank the associate editor and referees for their helpful comments, which have significantly improved this manuscript. The authors would also like to thank Assoc. Prof. Dr. Mehmet Yeşiltaş for the English language editing of the manuscript.

References

Altherr R, Holl A, Hegner E, Langer C, Kreuzer H (2000). High-potassium, calc-alkaline I-type plutonism in the European Variscides: northern Vosges (France) and northern Schwarzwald (Germany). Lithos 50: 51-73. doi: 10.1016/S0024-4937(99)00052-3

Altherr R, Siebel W (2002). I-type plutonism in a continental back-arc setting: Miocene granitoids and monzonites from the central Aegean Sea, Greece. Contributions to Mineralogy and Petrology 143: 397-415. doi: 10.1007/s00410-002-0352-y

Altınlı IE (1973). Bilecik Jurassic (Turkey). In: Doyran, S. (ed), Papers, Congress of Earth Sciences on the Occasion of the 50th Anniversary of the Turkish Republic. Ankara, Turkey: MTA Publication, pp. 105-114.

Altunkaynak Ş, Sunal G, Aldanmaz E, Genç CŞ, Dilek Y et al. (2012). Eocene Granitic magmatism in NW Anatolia (Turkey) revisited: new implications from comparative zircon SHRIMP U–Pb and 40Ar–39Ar geochronology and isotope geochemistry on magma genesis and emplacement. Lithos 155: 289-309. doi: 10.1016/j.lithos.2012.09.008

Annen C, Blund, J, Spark, RSJ (2006). The genesis of intermediate and silicic magmas in deep crustal hot zones. Journal of Petrology 47: 505-539. doi: 10.1093/petrology/egi084

Ayrton SN (1991). Appinites, lamprophyres and mafic microgranular enclaves: three related products of interaction between acid and basic magmas. In: Didier J, Barbarin B (eds). Enclaves and Granite Petrology. Developments in Petrology 13. Amsterdam, Netherlands: Elsevier, pp. 465-476.

Aysal N (2015). Mineral chemistry, crystallization conditions and geodynamic implications of the Oligo-Miocene granitoids in the Biga Peninsula, Northwest Turkey. Journal of Asian Earth Sciences 105: 68-84. doi: 10.1016/j.jseaes.2015.03.026

Aysal N, Keskin M, Peytcheva I, Duru O (2018). Geochronology, geochemistry and isotope systematics of a mafic–intermediate dyke complex in the İstanbul Zone. New constraints on the evolution of the Black Sea in NW Turkey. Geological Society, London, Special Publications 464 (1): 131-168. doi: 10.1144/SP464.4

Aysal N, Öngen S, Hanilçi N, Kasapçı C, Laçin D et al. (2020). Late magmatic – hydrothermal tourmaline occurrences within leucogranites in NW Anatolia (Turkey): mineral chemistry and genetic implications. Geochemistry (in press). https://doi: 10.1016/j.chemer.2020.125676

Aysal N, Ustaömer T, Öngen S, Keskin M, Köksal S et al. (2012). Origin of the Early-Middle Devonian magmatism in the Sakarya Zone, NW Turkey: geochronology, geochemistry and isotope systematics. Journal of Asian Earth Sciences 45: 201-222. doi: 10.1016/j.jseaes.2011.10.011

Bartoli O, Acosta-Vigil A, Ferrero S, Cesare B (2016). Granitoid magmas preserved as melt inclusions in high-grade metamorphic rock. American Mineralogist 101: 1543-1559. doi: 10.2138/am-2016-5541CCBYNCND

Baxter S, Feely M (2002). Magma mixing and mingling textures in granitoids: examples from the Galway Granite, Connemara, Ireland. Mineralogy and Petrology 76: 63-74. doi: 10.1007/s007100200032

Black KN, Catlos EJ, Oyman T, Demirbilek M (2013). Timing Aegean extension: evidence from in situ U–Pb geochronology and cathodoluminescence imaging of granitoids from NW Turkey. Lithos 180-181: 92-108. doi: 10.1016/j.lithos.2013.09.001

Blevin PL, Chappell BW (1992). The role of magma sources oxidation states and fractionation in determining the granite metallogeny of eastern Australia. Transactions of the Royal Society of Edinburgh: Earth Sciences 83: 305-316. doi: 10.1017/S0263593300007987

Castro A (2013). Tonalite–granodiorite suites as cotectic systems: a review of experimental studies with applications to granitoid petrogenesis. Earth-Science Reviews 124: 68-95. doi: 10.1016/j.earscirev.2013.05.006

Claeson DT, Meurer WP (2004). Fractional crystallization of hydrous basaltic "arc-type" magmas and the formation of amphibole-bearing gabbroic cumulates. Contributions to Mineralogy and Petrology 147: 288-304. doi: 10.1007/s00410-003-0536-0

Clarke DB (1995). Cordierite in felsic igneous rocks: a synthesis. Mineralogical Magazine 59: 311-325. doi: 10.1180/minmag.1995.059.395.15

Clemens JD (2006). Melting of the continental crust: fluid regimes, melting reactions, and source-rock fertility. In: Brown M, Rushmer T (eds.). Evolution and Differentiation of the Continental Crust. Cambridge, UK: pp. 296-327.

Clemens JD, Helps PA, Stevens G (2009). Chemical structure in granitic magmas – a signal from the source? Earth and Environmental Science Transactions of the Royal Society of Edinburgh 100: 159-172. doi:10.1130/2010.2472(11)

Clemens JD, Philips GN (2020). Granite suites: a problematic concept? Australian Journal of Earth Sciences. doi: 10.1080/08120099.2020.1701076.

Clemens JD, Stevens G (2012). What controls chemical variation in granitic magmas? Lithos 134-135: 317-329. doi: 10.1016/j.lithos.2012.01.001

Debon F, Le Fort P (1983). A chemical-mineralogical classification of common plutonic rocks and associations. Earth and Environmental Science Transactions of the Royal Society of Edinburgh 73 (3): 135-149. doi: 10.1017/S0263593300010117

Debon F, Le Fort, P (1988). A cationic classification of common plutonic rocks and their magmatic associations: principles, method, applications. Bulletin de Minéralogie 111 (5): 493-510.

Delaloye M, Bingöl E (2000). Granitoids from Western and Northwestern Anatolia: geochemistry and modelling of geodynamic evolution. International Geology Review 42: 241-268. doi: 10.1080/00206810009465081

Dias G, Leterrier J (1994). The genesis of felsic-mafic plutonic associations: a Sr and Nd isotopic study of the Hercynian Braga Granitoid Massif (Northern Portugal). Lithos 32: 207-223. doi: 10.1016/0024-4937(94)90040-X

Erdmann S, Scaillet B, Kellett DA (2010). Xenocryst assimilation and formation of peritectic crystals during magma contamination: an experimental study. Journal of Volcanology and Geothermal Research 198 (3-4): 355-367. doi: 10.1016/j.jvolgeores.2010.10.002

Ersoy EY, Palmer MR (2013). Eocene-Quaternary magmatic activity in the Aegean: implications for mantle metasomatism and magma genesis in an evolving orogeny. Lithos 180-181: 5-24. doi: 10.1016/j.lithos.2013.06.007

Ersoy EY, Palmer MR, Genç ŞC, Prelević D, Akal C et al. (2017). Chemo-probe into the mantle origin of the NW Anatolia Eocene to Miocene volcanic rocks: implications for the role of crustal accretion, subduction, slab roll-back and slab break-off processes in genesis of post-collisional magmatism. Lithos 288: 55-71. doi: 10.1016/j.lithos.2017.07.006

Farina F, Stevens G, Dini A, Rocchi S (2012). Peritectic phase entrainment and magma mixing in the late Miocene Elba Island laccolith–pluton–dyke complex (Italy). Lithos 153: 243-260. doi: 10.1016/j.lithos.2012.05.011

Foster MD (1960). Interpretation of the composition of trioctahedral micas: United States Geological Survey. Professional Paper 354 (B): 1-146.

Giret A, Bonin B, Leger JM (1980). Amphibole compositional trends in oversaturated and under saturated alkaline plutonic ring-complexes: Canadian Mineralogist 18: 481-495.

Gorton MW, Schandl ES (2000). From continents to island arcs: a geochemical index of tectonic setting for Arc-related and within-plate felsic to intermediate volcanic rocks. The Canadian Mineralogist 38 (5): 1065-1073. doi: 10.2113/gscanmin.38.5.1065

Harris NBW, Kelley S, Okay AI (1994). Post-collisional magmatism and tectonics in northwest Anatolia. Contributions to Mineralogy and Petrology 117: 241-252. doi: 10.1007/BF00310866

Hawkesworth CJ, Hergt JM, Ellam RM, McDermott F (1991). Element fluxes associated with subduction related magmatism. Philosophical Transactions of the Royal Society of London. Series A: Physical and Engineering Sciences 335: 393-405. doi: 10.1098/rsta.1991.0054

Henry DJ, Guidotti CV, Thomson JA (2005). The Ti-saturation surface for low-to-medium pressure metapelitic biotite: implications for geothermometry and Ti-substitution mechanisms. American Mineralogist 90: 316-328. doi: 10.2138/am.2005.1498

Hibbard MJ (1991). Textural anatomy of twelve magma-mixed granitoid systems: Enclaves and Granite Petrology. In: Didier J, Barbarin B (eds.). Developments in Petrology 13: 431-444.

Hibbard MJ (1995). Petrography to Petrogenesis. Jersey city?, NJ, USA: Prentice Hall.

Kamacı Ö, Altunkaynak Ş (2020). The role of accreted continental crust in the formation of granites within the Alpine style continental collision zone: geochemical and geochronological constrains from leucogranites in the Çataldağ Metamorphic Core Complex (NW Turkey). Lithos 354-355: 105347. doi: 10.1016/j.lithos.2019.105347

Keskin M (2002). FC-modeler: a Microsofts Excel® spreadsheet program for modelling Rayleigh fractionation vectors in closed magmatic systems. Computers and Geosciences 28: 919-928. doi: 10.1016/S0098-3004(02)00010-9

Köprübaşı N, Aldanmaz E (2004). Geochemical constraints on the petrogenesis of Cenozoic I-Type granitoids in northwestern Anatolia, Turkey: evidence for magma generation by lithospheric delamination in post-collisional setting. International Geology Review 46: 405-429. doi: 10.2747/0020-6814.46.8.705

Laurent O, Martin H, Moyen JF, Doucelance R (2014). The diversity and evolution of late-Archean granitoids: evidence for the onset of "modern-style" plate tectonics between 3.0 and 2.5 Ga. Lithos 205: 208-235. doi: 10.1016/j.lithos.2014.06.012

Leake BE, Woolley AR, Arps CES, Birch WD, Gilbert MC et al. (1997). Nomenclature of amphiboles: report of the subcommittee on amphiboles of the International Mineralogical Association. Commission on New Minerals and Mineral Names. Canadian Mineralogist 35: 219-246.

Liew TC, Hofmann A (1988). Precambrian crustal components, plutonic associations, plate environment of the Hercynian fold belt of Central Europe; indications from Nd and Sr isotopic study. Contributions to Mineralogy and Petrology 98: 129-138. doi: 10.1007/BF00402106

Maniar PO, Piccoli PM (1989). Tectonic discrimination of granitoids. Geological Society of America Bulletin 101: 635-643. doi: 10.1130/0016-7606(1989)101<0635:TDOG>2.3.CO;2

Moyen JF, Stevens G (2006). Experimental constraints on TTG petrogenesis: implications for Archean geodynamics. American Geophysical Union Geophysical Monograph Series 164, pp.149. doi: 10.1029/164GM11

Nakano S (1992). Internal textures and chemical compositions of anti-rapakivi mantled feldspars from Oki-Dogo Island, Japan. Mineralogy and Petrology 46: 123-135.

Okay AI, Tüysüz O (1999). Tethyan sutures of northern Turkey. Geological Society, London, Special Publications 156 (1): 475-515. doi: 10.1144/GSL.SP.1999.156.01.22

Okay AI, Noble PJ, Tekin UK (2011). Devonian radiolarian ribbon cherts from the Karakaya Complex, Northwest Turkey: implications for the Paleo-Tethyan evolution. Comptes Rendus Palevol 10 (1): 1-10. doi: 10.1016/j.crpv.2010.12.002

Palin RM, White RW, Green EC, Diener JF, Powell R et al. (2016). High grade metamorphism and partial melting of basic and intermediate rocks. Journal of Metamorphic Geology 34 (9): 871-892. doi: 10.1111/jmg.12212

Patiño Douce AE (1999). What do experiments tell us about the relative contributions of crust and mantle to the origin of granitic magmas? In: Castro A, Fernandez C, Vigneresse JL (eds.) Understanding granites. Integrating New and Classical Techniques. London, UK: Geological Society, Special Publication 168: 55-75. doi: 10.1144/GSL.SP.1999.168.01.05

Pearce JA (1983). Role of the sub-continental lithosphere in magma genesis at active continental margins. In: Hawkesworth CJ, Norry MJ (eds.). Continental Basalts and Mantle Xenolites. Nantwich, Shiva, 230-249.

Pearce JA, Bender JF, DeLong SE, Kidd WSF, Low PJ et al. (1990). Genesis of collision volcanism in Eastern Anatolia, Turkey. Journal of Volcanology and Geothermal Research 44 (1-2): 189-229. doi: 10.1016/0377-0273(90)90018-B

Pearce JA, Harris NBW, Tindle AG (1984). Trace element discrimination diagrams for the tectonic interpretation of granitic rocks. Journal of Petrology 25: 956-983. doi: 10.1093/petrology/25.4.956

Peccerillo R, Taylor SR (1976). Geochemistry of Eocene calc-alkaline volcanic rocks from the Kastamonu area. Northern Turkey. Contribution of Mineralogy and Petrology 58: 63-81. doi: 10.1007/BF00384745

Pe-piper G, Piper DJ (1989). Spatial and temporal variation in late Cenozoic back-arc volcanic rocks, Aegean Sea region. Tectonophysics 169 (1-3): 113-134. doi: 10.1016/0040-1951(89)90186-8

Putirka K (2016). Amphibole thermometers and barometers for igneous systems and some implications for eruption mechanisms of felsic magmas at arc volcanoes. American Mineralogist 101 (4): 841-858. doi: 10.2138/am-2016-5506

Rezaei-Kahkhaei M, Galindo C, Pankhurst RJ, Esmaeily D (2011). Magmatic differentiation in the calc-alkaline Khalkhab–Neshveh pluton, Central Iran. Journal of Asian Earth Sciences 42 (3): 499-514. doi: 10.1016/j.jseaes.2011.04.022

Ridolfi F, Renzulli A (2012). Calcic amphiboles in calc-alkaline and alkaline magmas: thermobarometric and chemometric empirical equations valid up to 1.130° C and 2.2 GPa. Contributions to Mineralogy and Petrology 163: 877-895. doi: 10.1007/s00410-011-0704-6

Ridolfi F, Renzulli A, Puerini M (2010). Stability and chemical equilibrium of amphibole in calc-alkaline magmas: an overview, new thermobarometric formulations and application to subduction-related volcanoes. Contributions to Mineralogy and Petrology 160: 45-66. doi: 10.1007/s00410-009-0465-7

Rudnick RL, Gao S (2003). Composition of the continental crust. In: Rudnick RL (ed.). The crust, Treatise on Geochemistry 3: 1-64. doi: 10.1016/B0-08-043751-6/03016-4

Shand SJ (1943). Eruptive Rocks. London, UK: T. Murby

Stevens G, Villaros A, Moyen JF (2007). Selective peritectic garnet entrainment as the origin of geochemical diversity in S-type granites. Geology 35 (1): 9-12. doi: 10.1130/G22959A.1

Streckeisen AL, Le Maitre RW (1979). A chemical approximation to the modal QAPF classification of the igneous rocks. Neues Jahrbuch fur Mineralogie, Abhandlungen 136: 169-206.

Sun SS, McDonough WF (1989). Chemical and isotopic systematics of oceanic basalts: Implications for mantle composition and processes. In: Saunders AD, Norry MJ (eds.). Magmatism in the Ocean Basins. Geological Society London Special Publication 42: 313-345. doi: 10.1144/GSL.SP.1989.042.01.19

Taylor J, Stevens G (2010). Selective entrainment of peritectic garnet into S-type granitic magmas: evidence from Archaean mid-crustal anatectites. Lithos 120 (3-4): 277-292. doi: 10.1016/j.lithos.2010.08.015

Thompson AB (1982). Dehydration melting of pelitic rocks and the generation of H_2O-undersaturated granitic liquids. American Journal of Science 282: 1567-1595. doi:10.2475/ajs.282.10.1567

Tindle AG, Pearce JA (1981). Petrogenetic modelling of in situ fractional crystallization in the zoned Loch Doon pluton, Scotland. Contributions to Mineralogy and Petrology 78: 196-207. doi: 10.1007/BF00373781

Vegas N, Rodriguez J, Cuevas J, Siebel W, Esteban JJ et al. (2011). The sphene-centered ocellar texture: an effect of grain-supported flow and melt migration in a hyperdense magma mush. The Journal of Geology 119 (2): 143-157. doi: 10.1086/658200

Villaseca C, Barbero L, Herreros V (1998). A re-examination of the typology of peraluminous granite types in intracontinental orogenic belts. Transactions of the Royal Society of Edinburgh: Earth Sciences 89 (2): 113-119. doi: 10.1017/S0263593300007045

Walker AJ, Carr JM (1986). Compositional variations caused by phenocryst sorting at Cerro Negro volcano, Nicaragua. Geological Society of America 97 (9): 1156-1162. doi: 10.1130/0016-7606(1986)97<1156:CVCBPS>2.0.CO;2

Wones DR (1989). Significance of the assemblage titanite + magnetite + quartz in granitic rocks. American Mineralogist 74 (7-8): 744-749.

Yakymchuk C (2019). On granites. Journal Geological Society of India 94: 9-22. doi: 10.1007/s12594-019-1261-2

Yılmaz Şahin S, Aysal N, Güngör Y (2012). Petrogenesis of late cretaceous adakitic magmatism in the İstanbul zone (Çavuşbaşı Granodiorite, NW Turkey). Turkish Journal of Earth Sciences 21 (6): 1029-1045. doi: 10.3906/yer-1005-15

Zhou ZX (1986). The origin of intrusive mass in Fengshandong, Hubei province. Acta Petrologica Sinica 2: 59-70.

Zhu Y, Lai SC, Qin JF, Zhu RZ, Zhang FY et al. (2020). Petrogenesis and geochemical diversity of Late Mesoproterozoic S-type granites in the western Yangtze Block, South China: co-entrainment of peritectic selective phases and accessory minerals. Lithos 352-353: 105326. doi: 10.1016/j.lithos.2019.105326